

A Corrosion Model for Production Tubing

A thesis presented to  
the faculty of  
the Russ College of Engineering and Technology of Ohio University

In partial fulfillment  
of the requirements for the degree  
Master of Science

Kyle A. Addis

December 2014

© 2014 Kyle A. Addis. All Rights Reserved.

This thesis titled  
A Corrosion Model for Production Tubing

by  
KYLE A. ADDIS

has been approved for  
the Department of Chemical and Biomolecular Engineering  
and the Russ College of Engineering and Technology by

Srdjan Nesic  
Professor of Chemical and Biomolecular Engineering

Dennis Irwin  
Dean, Russ College of Engineering and Technology

## ABSTRACT

ADDIS, KYLE A., M.S., December 2014, Chemical Engineering

A Corrosion Model for Production Tubing

Director of Thesis: Srdjan Nesic

Over the years there have been many attempts to model the corrosion process as it relates to oil and gas production and transportation. Most of these models were created for use in transportation lines, with relatively few attempts to model corrosion at reservoir conditions. Many of these models failed to account for the complexities and non-idealities present at such extreme conditions. Thus, the purpose of this research is to create a model for the corrosion of production tubing.

The Institute for Corrosion and Multiphase Technology's (ICMT) FREECORP model was used as a basis for the production tubing model, here called WELLCORP. The original FREECORP model was first modified to account for non-idealities in the gas and liquid phases. This model was then used to simulate production data and calculate wall thickness loss. The calculated wall thickness losses were then compared to wall losses measured by caliper readings. An additional thermodynamic model, ThermoCORP, was created from the open literature and previous ICMT work to predict corrosion product stability.

## DEDICATION

*To*

*my wife, Thu Tran Addis*

*my parents, Tony and Kim Addis*

*my brother, Josh Addis*

*my grandparents, Barton & Donna Addis and Wayne & Carol Harmon*

*and my teachers, professors, and mentors*

## ACKNOWLEDGMENTS

I would like to thank my advisor Dr. Srdjan Nesic, project leaders Dr. Bruce Brown and Dr. Marc Singer, and Dr. David Young for their direction and support throughout my studies. I would like to also thank the technical staff at the Institute for Corrosion and Multiphase Technology, especially Al Shubert and Garret Brown for programming help and advice. Finally, I would like to thank ConocoPhillips for financial support, and specifically Dr. Mohsen Achour, Dr. Sonja Richter, and Dr. Raymundo Case for their expert advice and support.

## TABLE OF CONTENTS

Abstract.....	3
Dedication.....	4
Acknowledgments.....	5
List of Tables .....	8
List of Figures.....	9
Chapter 1: Introduction.....	12
Chapter 2: Literature Review.....	14
2.1 The Corrosion Process .....	14
2.2 Modeling Corrosion .....	15
2.3 Parameters Affecting Production Tubing Corrosion.....	17
2.3.1 Volumetric Flow Rates .....	19
2.3.2 Flow Regime.....	19
2.3.3 Brine Composition .....	20
2.3.4 Gas Composition.....	21
2.3.5 Temperature and Pressure.....	22
2.3.6 Tubing Size and Properties .....	23
2.4 Issues with Modeling Production Tubing Corrosion .....	23
2.4.1 Conditions.....	23
2.4.2 Non-Idealities.....	24
2.4.3 Lack of Accurate Data .....	24
Chapter 3: Objectives .....	26
3.1 Objectives.....	26
Chapter 4: Wellcorp Corrosion Model .....	27
4.1 FREECORP.....	27
4.2 WELLCORP .....	31
4.2.1 Input Parameters .....	31
4.2.2 Output Parameters.....	32
4.2.3 Important Assumptions.....	32
4.2.4 Equation of State.....	33

4.2.5	Fugacity Coefficient.....	35
4.2.6	CO <sub>2</sub> Solubility.....	37
4.2.7	H <sub>2</sub> S Solubility .....	40
4.2.8	Activity Coefficient .....	43
4.2.9	Ferrous (Fe <sup>2+</sup> ) Ion Concentration Calculation .....	46
4.2.10	Water Condensation Rate Calculation .....	47
4.2.11	Flow Model.....	50
4.2.12	Material Guidance.....	51
4.3	Program Design and Structure .....	52
4.3.1	Line Model.....	52
4.3.2	Single Day Run.....	57
4.3.3	Production Data Analysis .....	61
4.4	Results and Discussion.....	64
4.4.1	FREECORP Improvements .....	64
4.4.2	Analysis of Field Data .....	66
4.4.3	Model Results .....	70
4.5	Summary .....	74
4.5.1	Model Limitations.....	74
4.5.2	Model Achievements .....	75
Chapter 5:	ThermoCORP .....	76
5.1	Methodology .....	76
5.2	Interface and Design.....	78
5.3	Results and Discussion.....	80
5.4	Summary .....	86
Chapter 6:	Conclusions and Future Work .....	88
6.1	Conclusions .....	88
6.2	Future Work .....	89
References	.....	90

## LIST OF TABLES

Table 1: Interaction parameters for Duan-Sun CO <sub>2</sub> model [39].....	39
Table 2: Parameter limits for Duan-Sun CO <sub>2</sub> Solubility Model [39] .....	40
Table 3: Interaction parameters for Duan et al. H <sub>2</sub> S model [41] .....	42
Table 4: Parameter limits for Duan et al. H <sub>2</sub> S solubility model [41].....	42
Table 5: Electrolyte parameters for Pitzer activity model .....	45
Table 6: WELLCORP class description .....	55
Table 7: Public methods of the LineModel class.....	56
Table 8: Public methods of the PointModel class.....	56
Table 9: Public methods of the AnodicReaction and CathodicReaction classes.....	57
Table 10: Public methods of the FlowModel class.....	57

## LIST OF FIGURES

Figure 1: Diagram of a typical production well. Adapted from Manocha and Carter [13]. .....	18
Figure 2: Diagram of flow regimes in downhole tubing, where blue represents liquid and white represents gas. Adapted from Shoham [18].	20
FREECORP predicts corrosion rates quite accurately at low partial pressures of CO <sub>2</sub> , but it begins to overestimate corrosion once the partial pressure of CO <sub>2</sub> surpasses 10 bars, as shown in Figure 3. This could be due to Henry's Law overestimating the CO <sub>2</sub> concentration in the liquid phase, or the precipitation of iron carbonate, which could have affected the experimental results plotted in Figure 3. This shows a lower corrosion rate than was predicted with FREECORP at high pCO <sub>2</sub> .	30
Figure 4: Comparison of Duan-Sun CO <sub>2</sub> solubility model with Henry's Law	40
Figure 5: Comparison of Duan et al. H <sub>2</sub> S solubility model with Henry's Law	43
Figure 6: Comparison of Pitzer activities for H <sup>+</sup> , OH <sup>-</sup> , and HCO <sub>3</sub> <sup>-</sup>	46
Figure 7: Water content of natural gas. Produced with the Bukacek correlation [43]	49
Figure 8: NACE MR0175 SSC zone map. Adapted from NACE MR0175 standard [30]. .....	52
Figure 9: Schematic of a line model	53
Figure 10: WELLCORP main calculation algorithm	54
Figure 11: WELLCORP program structure	56
Figure 12: Schematic of single day run algorithm	58

	10
Figure 13: WELLCORP interface .....	59
Figure 14: Advanced gas input window .....	59
Figure 15: Advanced brine input window .....	60
Figure 16: Flow model input window.....	60
Figure 17: Schematic of production data analysis.....	62
Figure 18: Interface for WELLCORP production data analysis.....	63
Figure 19: Example of data analysis production cumulative wall loss result.....	63
Figure 20: Comparison between corrosion models and experimental data, at 60°C, pH 5.0, 1 m/s, 1 wt% NaCl. Experimental data take from Wang et al. [21]. .....	65
Figure 21: Comparison between corrosion models and experimental data, at 80 bar CO <sub>2</sub> , 25°C, pH 3.0, 1 m/s, 1 wt% NaCl. Experimental data take from Nor et al. [46].....	66
Figure 22: Normalized caliper data for Well A .....	68
Figure 23: Normalized caliper data for Well B .....	68
Figure 24: Normalized caliper data for Well C .....	69
Figure 25: Normalized caliper data for Well D .....	70
Figure 26: Normalized caliper and model results comparison for Well A.....	71
Figure 27: Normalized caliper and model results comparison for Well B. ....	72
Figure 28: Normalized caliper and model results comparison for Well C. ....	73
Figure 29: Normalized caliper and model results comparison for Well D.....	74
Figure 30: Pourbaix diagram interface. An example is shown for a pure H <sub>2</sub> S system.....	79
Figure 31: "Slice" diagram interface. Shown is an example for a pure H <sub>2</sub> S system with varied temperature. ....	80

Figure 32: Pourbaix diagram comparison for an Fe-H <sub>2</sub> O system at 25°C, [Fe <sup>2+</sup> ]=10ppm, [Fe <sup>3+</sup> ]=10 <sup>-6</sup> mol/L .....	81
Figure 33: Pourbaix diagram comparison for an Fe-H <sub>2</sub> O system at 80°C, [Fe <sup>2+</sup> ]=10ppm, [Fe <sup>3+</sup> ]=10 <sup>-6</sup> mol/L .....	82
Figure 34: Pourbaix diagram comparison for an Fe-H <sub>2</sub> O-H <sub>2</sub> S system at 25°C, 10% H <sub>2</sub> S, [Fe <sup>2+</sup> ]=10ppm, [Fe <sup>3+</sup> ]=10 <sup>-8</sup> mol/L .....	83
Figure 35: Pourbaix diagram comparison for an Fe-H <sub>2</sub> O-H <sub>2</sub> S system at 80°C, 10% H <sub>2</sub> S, [Fe <sup>2+</sup> ]=10ppm, [Fe <sup>3+</sup> ]=10 <sup>-8</sup> mol/L .....	83
Figure 36: Pourbaix diagram comparison for an Fe-H <sub>2</sub> O-H <sub>2</sub> S system at 250°C, 10% H <sub>2</sub> S, [Fe <sup>2+</sup> ]=10ppm, [Fe <sup>3+</sup> ]=10 <sup>-8</sup> mol/L .....	84
Figure 37: Pourbaix diagram comparison for an Fe-H <sub>2</sub> O-CO <sub>2</sub> system 25°C, 1 bar CO <sub>2</sub> , [Fe <sup>2+</sup> ]=10ppm, [Fe <sup>3+</sup> ]=10 <sup>-6</sup> mol/L .....	85
Figure 38: Pourbaix diagram comparison for an Fe-H <sub>2</sub> O-CO <sub>2</sub> system 80°C, 2.21 bar CO <sub>2</sub> , [Fe <sup>2+</sup> ]=10ppm, [Fe <sup>3+</sup> ]=10 <sup>-6</sup> mol/L .....	85
Figure 39: Pourbaix diagram comparison for an Fe-H <sub>2</sub> O-CO <sub>2</sub> system 250°C, 2.43 bar CO <sub>2</sub> , [Fe <sup>2+</sup> ]=10ppm, [Fe <sup>3+</sup> ]=10 <sup>-6</sup> mol/L .....	86

## CHAPTER 1: INTRODUCTION

Carbon dioxide (CO<sub>2</sub>) and hydrogen sulfide (H<sub>2</sub>S) corrosion are a significant problem in oil and gas production and transportation (transmission and distribution) systems [1]. Downhole corrosion in oil and gas production systems has received significant attention due to the high CO<sub>2</sub> and H<sub>2</sub>S content in the produced fluids that can cause failure of production tubing. Modeling has contributed a great deal to understanding and mitigating the corrosion problem. Until now, it has been common practice to use the de Waard-Milliams correlation for corrosion prediction [1]. This correlation, however, is not intended for well applications, and does not account for the range of environmental parameters in well conditions, such as high pressure, high temperature, and the presence of H<sub>2</sub>S. A better prediction tool is needed, if possible a mechanistic model similar to ICMT's FREECORP corrosion prediction model used in transport pipeline conditions. FREECORP does not predict corrosion rates well at high temperatures and pressures, nor does it account for other factors, such as non-idealities and corrosion product stability. The purpose of this study is to develop an improved model for production tubing corrosion prediction, here called WELLCORP, by modifying the FREECORP model to predict corrosion rates and corrosion products at reservoir conditions.

This thesis is structured as follows: Chapter 2 provides a review of the key literature relating to aqueous corrosion of steel, and some models for corrosion prediction specifically related to production tubing. Chapter 3 outlines the research objectives and hypotheses. Chapter 4 describes the improvements made to FREECORP in the creation

of the production tubing corrosion model, WELLCORP, as well as a comparison to field measurements, and a discussion of the results. Chapter 5 provides a description of the Pourbaix diagram generation program, ThermoCORP, and compares the results with a commercial Pourbaix diagram generator. Finally, Chapter 6 summarizes the findings of this research, and provides suggestions for future research.

## CHAPTER 2: LITERATURE REVIEW

Corrosion has been a challenge for the oil and gas industry for many years, and as operators use deeper wells, it becomes more problematic [1]. As well conditions become more extreme, corrosion models become an invaluable resource for maintaining safe and reliable operation. Many of the models used in the oil and gas industry for corrosion rate prediction have been developed using laboratory and field data at transport pipeline conditions [2]–[5]. These models provide accurate predictions of corrosion rates at low temperatures (<80°C) and low pressures (<20 bar), but do not provide adequate results above these conditions, as seen in downhole operations.

### 2.1 The Corrosion Process

Corrosion occurs in an aqueous environment when a metal, in this case iron, dissolves by anodic reaction, and hydrogen is produced by cathodic reaction. This process is characterized by the following reactions in a CO<sub>2</sub> environment:

Dissolution of CO<sub>2</sub>:



Hydration of CO<sub>2</sub>:



Dissociation of carbonic acid:



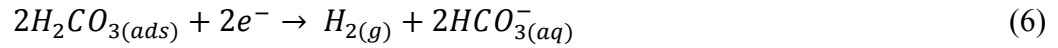
Dissociation of bicarbonate ions:



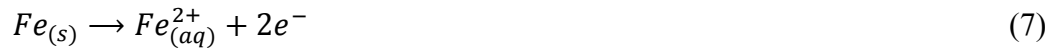
Reduction of hydrogen ions:



Direct reduction of carbonic acid:



Oxidative dissolution of iron:



If hydrogen sulfide (H<sub>2</sub>S) is present, the following reactions occur in addition to the above reactions:

Dissolution of H<sub>2</sub>S:



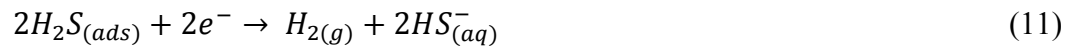
Dissociation of aqueous H<sub>2</sub>S:



Dissociation of bisulfide:



Direct reduction of H<sub>2</sub>S:



## 2.2 Modeling Corrosion

One of the first attempts to model the CO<sub>2</sub> corrosion process was performed by de Waard and Milliams [6], [7]. They suggested a simple means to calculate corrosion rate from temperature and partial pressure of CO<sub>2</sub> using a nomogram. This idea was expanded by de Waard *et al.* to include flow, and by de Waard and Lotz to include pH [8], [9].

These models were initially mechanistic, but in later versions became more empirical. This empiricism restricts the accuracy and applicability of the predictions to a limited range of conditions used for calibration.

In 1996, Nesic *et al.* proposed a mechanistic model which not only considered the above mentioned parameters, but also chemical and electrochemical reactions [2]. This model, however, still did not take into account the formation of corrosion product layers, nor did it include H<sub>2</sub>S corrosion. It also assumed an ideal gas phase, which is not suitable for the high temperatures and pressures present in downhole corrosion. This model was modified several times, and now considers many of the elements missing from the original version. Recent work by Zheng *et al.* has included a new electrochemical model for H<sub>2</sub>S corrosion [10], [11].

In 2003, Nordsveen *et al.* and Nesic *et al.* introduced an advanced model, known as MULTICORP, which included the diffusion of species, electromigration, and precipitation of surface layers [3]–[5]. This model took into account the formation of surface layers, which allowed for a more accurate prediction of corrosion rates in film forming conditions. It did not, however, include any failure mechanism of those layers. Like the previous model, this model was modified over the years, and is now one of the leading tools for predicting corrosion rates. However, it still does not predict downhole corrosion rates well due to its calibration with laboratory data at low temperatures and pressures.

An improved model is still needed—one that can accurately predict downhole corrosion. The base model used in this study is an updated version of the model by Nesic

*et al.*, known as FREECORP<sup>1</sup> [2]. An overview of the model and the improvements to be added to this model are detailed in Chapter 4.

### **2.3 Parameters Affecting Production Tubing Corrosion**

Production tubing refers to the steel tube connecting the reservoir to the wellhead (Figure 1). The tubing near the reservoir is exposed to high pressure and high temperature, on the order of 140°C and 530 bar or even greater [12]. These conditions vary from well to well. As wells become depleted, the pressure of the well decreases. In addition, the composition of each well can vary greatly. Some gas wells may contain mostly acid gases (i.e. CO<sub>2</sub> and H<sub>2</sub>S) while others may contain mostly hydrocarbons.

---

<sup>1</sup> Available at <http://www.corrosioncenter.ohiou.edu/software/freecorp>

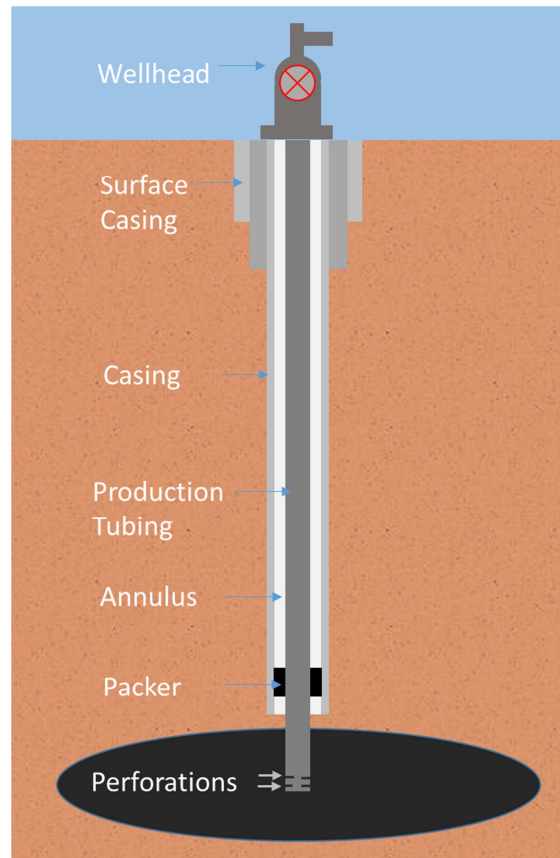


Figure 1: Diagram of a typical production well. Adapted from Manocha and Carter [13].

The casing is a steel pipe cemented in place inside the hole. This casing helps to prevent the wellbore from collapsing, and controls the flow of fluids during completion. Several layers of casing can be present near the surface. The production tubing is the steel tube through which production fluids flow. The annulus is the gap between the casing and the production tubing. The space can sometimes be used for production, or for the injection of fluids. The wellhead is the surface termination of the wellbore and is used for pressure and flow control. A packer is a mechanical device that provides a seal between the casing and the production tubing, which isolates the annulus. The packer is used to control the annulus conditions; production/injection therein is controlled with the packer.

Having introduced the anatomy of a production well, the key operational parameters affecting corrosion can be discussed. In the following sections, some of the important factors affecting production tubing corrosion in particular will be discussed. These factors will be addressed in Chapter 4 in terms of corrosion modeling.

### 2.3.1 Volumetric Flow Rates

The volumetric flow rates of oil, gas, and water are important parameters for calculating the velocity of each phase. Water velocity has a direct impact on the extent of corrosion via mass transfer [14]. Additionally, high liquid velocities can lead to the removal of corrosion product layers and, if sand is present, erosion [4], [15]. The gas flow-rate is also used to calculate the amount of water that condenses along the tubing. These are commonly and accurately measured parameters, as they directly impact the profit of the producer.

### 2.3.2 Flow Regime

The flow regime is another factor that can have a drastic effect on corrosion rates [16]. It is suggested that flow can transition between several flow regimes during its ascent in the tubing [17]. There are, however, three common flow regimes in downhole tubing, as shown in Figure 2: bubbly, slug/churn (intermittent), and annular-mist. In bubbly flow the pipe is filled with liquid that contains many dispersed bubbles. If there are intermittent pockets of large gas bubbles in between slugs of the liquid phase, it is referred to as slug/churn flow. The last case, annular-mist flow, occurs when the liquid

phase flows near the wall of the pipe and the gas phase carrying small droplets flows through the center of the pipe. The FREECORP model assumes simple single-phase flow—a pipe filled entirely with liquid.

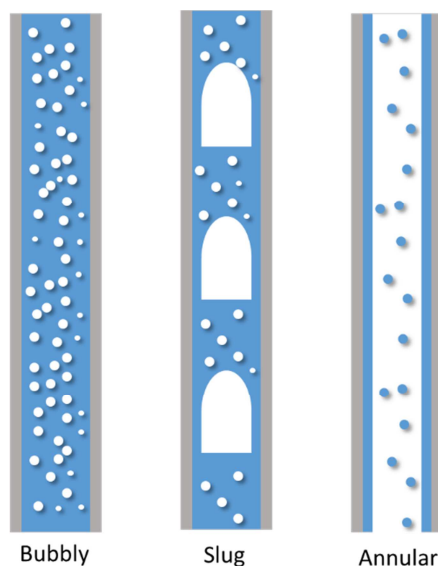


Figure 2: Diagram of flow regimes in downhole tubing, where blue represents liquid and white represents gas. Adapted from Shoham [18].

### 2.3.3 Brine Composition

The brine composition is an important parameter, but is not often reported for wells. It is, however, important for making accurate corrosion predictions. This is because the composition of the produced water affects the way in which aqueous species interact. High concentrations of salt can lead to localized corrosion but also to a decrease in general corrosion rate [19]. Since some fields can have upwards of 200,000 ppm of chlorides in the produced water, chlorides need to be accounted for in the model [12].

The acidity of the brine is often specified in terms of alkalinity, as in situ pH cannot be directly measured accurately in the well. Total alkalinity is the amount of acid required to neutralize the produced water from the well. It is usually measured in a lab by titration. The pH endpoint can vary depending on the procedure and indicator used, but typically it is between around pH 5.1 and pH 4.5 [20]. This quantifies the acid-reducing power of the produced water, and is generally reported as bicarbonate equivalent ( $\text{HCO}_3^-$ ). Total alkalinity is an important factor in pH calculations. Often there are organic acids present in the brine which, even at low concentrations, can have a major impact on the corrosion rate [21].

#### 2.3.4 Gas Composition

The composition of the gas stream has a significant impact on the corrosion inside a well, as it directly affects water composition. At minimum, the concentration of  $\text{CO}_2$  and  $\text{H}_2\text{S}$  should be reported, but if the full composition of gas is provided a more accurate characterization is possible. The partial pressures of  $\text{CO}_2$  and  $\text{H}_2\text{S}$  directly influence the concentration of corrosive species in solution, and thus corrosion rates inside the tubing [10], [22]. Some fields are highly “sour”, upwards of 20 % or more  $\text{H}_2\text{S}$ , in addition to having high concentrations of  $\text{CO}_2$  (40 % or more) in the gas phase [12]. The other inert species (from a corrosion standpoint), such as methane, ethane, etc., affect the gas physical properties such as: density, viscosity etc. These parameters in turn affect gas velocity, though the FREECORP model does not take this effect into account.

### 2.3.5 Temperature and Pressure

Temperature has been shown to be an important factor in the corrosion process, and was one of variables included in the original de Waard-Milliams corrosion model [6], [7]. In the absence of corrosion product layers, high temperatures generally lead to higher corrosion rates, while low temperatures lead to lower corrosion rates [19], [23]. Additionally, downhole and wellhead temperature affects many other physical properties of the fluid along the well, such as: gas densities, acid-gas solubilities, chemical equilibria including corrosion product layer formation, typically iron carbonate – often referred to as siderite [24]. If the temperature is high enough, a protective magnetite ( $\text{Fe}_3\text{O}_4$ ) layer can form, lowering corrosion rate significantly [25]. In the presence of  $\text{H}_2\text{S}$ , an iron sulfide layer is typically present [26], [27]. Iron carbonate and iron sulfide layers are the only types of corrosion product layer accounted for in the FREECORP model.

Total pressure has little direct effect on the corrosion process, but is directly affecting the partial pressures of  $\text{CO}_2$  and  $\text{H}_2\text{S}$ , which have a major influence on the corrosion rate [23], [27]. The downhole and wellhead pressures are used for calculating the pressure gradient along the tubing, and for following the change in partial pressures of  $\text{CO}_2$  and  $\text{H}_2\text{S}$  along the well. Pressure also affects the gas density, and in turn has an effect on the gas velocity.

High pressures and high temperatures become an issue when modeling due to the non-idealities of the gas phase. FREECORP uses Henry's Law to calculate  $\text{CO}_2$  and  $\text{H}_2\text{S}$  aqueous concentrations, similar to the original MULTICORP model [3]. However, at downhole conditions, these simple idealized calculations diverge from real behavior.

Downhole conditions are well outside the calculation limits of the current FREECORP model [10].

### 2.3.6 Tubing Size and Properties

The tubing inner diameter is used to convert the volumetric flow rates to velocities. The length of the tubing is used to calculate temperature and pressure profiles. In addition to the size of the tubing, the composition and properties of the steel used to make tubing are also important. Recently, Akeer *et al.* showed that different heat treatments (normalized, quenched, and tempered), metallurgy, and microstructures of carbon steel have an impact on the localized corrosion of carbon steels [28]. In the presence of H<sub>2</sub>S, harder steels may be susceptible to sulfide stress cracking; thus, a nickel-based alloy such as Hastelloy C-276 may be required [29]. Carbon steels and corrosion resistant alloys (CRAs) have very different corrosion rates. The materials used for downhole tubing and casing are subject to the NACE MR0175 standard which provides guidance on material hardness and yield strength [30]. All field data in this work are from fields using API L-80, J-55, and J-65 steels. Most experimental data is acquired using an X-65 steel.

## 2.4 Issues with Modeling Production Tubing Corrosion

### 2.4.1 Conditions

Conditions in wells are often much harsher than those in the transportation lines [12]. In addition, a wide range of operational conditions can be encountered.

Temperatures and pressures are often much higher, and can range from below freezing at the wellhead to well beyond 200°F, depending on the geographic location of the well. Pressures can range from atmospheric pressure (14.5 psi) to more than 10,000 psi. Additionally, the presence of oil can have a dramatic impact on the corrosion rate of the system due to wetting effects, as well as the inhibition effects of crude oil [1], [31].

#### 2.4.2 Non-Idealities

At some of the more extreme well conditions mentioned above (high pressure), the gas phase does not act in an ideal manner. This is due to the gas molecules interacting with each other and departure from the concept of an ideal gas is seen. Because of these interactions a more robust equation of state is required to perform the calculations. Pressure is replaced by fugacity, which can be seen as an “effective” pressure, which accounts for intermolecular interaction [32], [33]. In addition to the non-idealities in the gas phase, there are also non-idealities in the produced water. These non-idealities arise due to the high concentrations of ions in the produced water, which are caused by the interaction of species in the solution. To account for this, concentrations must be replaced by activities, which can be thought of as effective concentrations [32], [34], [35].

#### 2.4.3 Lack of Accurate Data

The final difficulty is related to the overall accuracy of the data available about critical parameters. Production rates are averaged either on a daily or monthly basis, so shorter periods of high or low production are often not included. The composition of the

produced water and gas phase may only be measured a limited number of times during the lifetime of the well [36]. These compositions could change greatly over the lifetime of the well. The pressure and temperature profile are also estimated since the true profile is unknown; they are often assumed to change linearly along the tubing. Additionally, pH must be estimated from alkalinity since it cannot be directly measured. There have been attempts recently by Plennevaux *et al.* to improve pH calculations at downhole conditions [37]. This approach makes use of a modified Henry's Law, but can be further improved upon.

In addition to the inaccuracy of production data, the wall thickness losses of production tubing reported by in-line inspection techniques are often inaccurate. The accuracy of the so called caliper data is typically 70-80 % [38]. More accurate techniques are available to measure pipe thickness wall loss in transport lines (e.g. intelligent pigging), but since tubing is buried deep with no access to the bottom-hole end, the only available technique for wall loss measurement is a caliper survey.

This review of current literature indicates there are many complexities associated with production tubing corrosion that are unaccounted for in the present model, such as species fugacities/activities, thermodynamic stabilities, and flow physics. The objective of this research is to address some of these complexities, and to compare the improved model with field and experimental data.

## CHAPTER 3: OBJECTIVES

### 3.1 Objectives

The literature review shows several factors that make modeling of production tubing corrosion problematic. The goal of this research is to account for these deficiencies in the newly built WELLCORP model. The specific objectives of this research project are as follows:

- Create a line model using FREECORP point model as the kernel.
- Replace the ideal gas equation with the Peng-Robinson equation of state.
- Add fugacity ( $\phi$ ) and activity coefficients ( $\gamma$ ) to phase calculations.
- Replace Henry's Law with improved solubility models.
- Calculate water drop-out along the tubing.
- Add a vertical multiphase flow model to replace the simple full liquid pipe model.
- Include a calculated ionic strength value to replace the constant value in FREECORP.
- Predict corrosion product layer formation.
- Validate the model using experimental and field data.
- Provide guidance for allowable materials based on the NACE MR0175/ISO 15156 standard.

## CHAPTER 4: WELLCORP CORROSION MODEL

The following sections detail the modifications implemented in order to adapt the FREECORP point model into a WELLCORP line model. These sections will introduce FREECORP, and detail the improvements made to the model, as well as the new features.

### 4.1 FREECORP

The current corrosion model in FREECORP is based on the mechanistic model developed by Netic *et al.* [2]. The original model has been modified to include H<sub>2</sub>S, acetic acid (HAc), and scaling effects [3]–[5], [27]. This model is coded in Visual Basic for Applications (VBA) using Microsoft Excel. All the equations and methods used in FREECORP are from the open literature, the VBA code is available to the user via the Visual Basic Developer window.

FREECORP begins the corrosion calculation process by calculating the current density (which is equivalent to a corresponding mass flux) for each cathodic reaction in the corrosion process [10]. Each cathodic species' current density can be separated into a charge transfer, and a limiting current portion:

$$\frac{1}{i_c} = \frac{1}{i_{ct}} + \frac{1}{i_{lim}} \quad (12)$$

Where:

$i_c$ : total cathodic current density for a species, A/m<sup>2</sup>;

$i_{ct}$ : charge transfer current density, A/m<sup>2</sup>;

$i_{lim}$ : limiting current density, A/m<sup>2</sup>.

These current densities from different species are then summed and set equal to the anodic current density (Equation 11), what can be seen as a charge balance equation at the corroding surface where the reduction/oxidation (cathodic/anodic) processes are happening.

$$i_{c(H^+)} + i_{c(H_2CO_3)} + i_{c(HAc)} + i_{c(O_2)} + i_{c(H_2O)} = i_{a(Fe)} \quad (13)$$

Once this equation is solved for the corrosion potential, each current density term can be calculated. The corrosion current density is set equal to the anodic current density:

$$i_{corr} = i_{a(Fe)} \quad (14)$$

Finally, using Faraday's Law, the corrosion current density is converted to a corrosion rate:

$$CR = \frac{i_{corr} M_{Fe}}{\rho_{Fe} n F} \quad (15)$$

Where:

$M_{Fe}$ : Molar mass of iron, g/mol;

$\rho_{Fe}$ : Density of iron, g/m<sup>3</sup>;

$n$ : Number of electrons released ( $n=2$  for iron);

$F$ : Faraday's Constant.

In the presence of H<sub>2</sub>S, an alternative calculation is used [10]; this is due to the assumption that a mackinawite (FeS) corrosion product layer is always present. Thus, the corrosion process is assumed to be always under mass transfer control. The corrosion rate is determined by the flux of corrosive species through the layer. The general equation for the flux of species through this film is shown in Equation 16, where  $i$  represents H<sub>2</sub>S, CO<sub>2</sub>, HAc, or H<sup>+</sup>.

$$Flux_j = A_j \ln \frac{c_j - Flux_j \left( \frac{\delta_{OS}}{D_j \varepsilon \psi} + \frac{1}{k_{m(j)}} \right)}{c_{s(j)}} \quad (16)$$

Where:

$Flux_j$ : Flux of species  $j$ , mol/(m<sup>2</sup>s);

$A_j$ : Experimentally determined constant for solid state diffusion;

$c_j$ : Bulk concentration of species  $j$ , mol/m<sup>3</sup>;

$\delta_j$ : Thickness of outer scale, m;

$D_j$ : Diffusion coefficient for species  $j$  in water, m<sup>2</sup>/s;

$\varepsilon$ : Porosity of outer mackinawite scale;

$\psi$ : Tortuosity of outer mackinawite scale;

$k_{m(j)}$ : Mass transfer coefficient of species in liquid boundary layer, m/s;

$c_{s(j)}$ : Surface concentration of species  $j$ , mol/m<sup>3</sup>.

With the flux of each species through the layers calculated, the fluxes can be converted easily to a corrosion rate (Equation 17). After which the corrosion rate can be converted to the required units.

$$CR_{tot} = (Flux_{H_2S} + Flux_{H^+} + Flux_{HAc} + Flux_{CO_2}) \frac{M_{Fe}}{\rho_{Fe}} \quad (17)$$

Where:

$CR_{tot}$ : Total corrosion rate, m/s;

$Flux$ : Flux of H<sub>2</sub>S, H<sup>+</sup>, HAc, CO<sub>2</sub> calculated in Equation 16, mol/(m<sup>2</sup>s);

$M_{Fe}$ : Molar mass of iron, g/mol;

$\rho_{Fe}$ : Density of iron, g/m<sup>3</sup>.

FREECORP predicts corrosion rates quite accurately at low partial pressures of  $\text{CO}_2$ , but it begins to overestimate corrosion once the partial pressure of  $\text{CO}_2$  surpasses 10 bars, as shown in Figure 3. This could be due to Henry's Law overestimating the  $\text{CO}_2$  concentration in the liquid phase, or the precipitation of iron carbonate, which could have affected the experimental results plotted in Figure 3. This shows a lower corrosion rate than was predicted with FREECORP at high  $\text{pCO}_2$ .

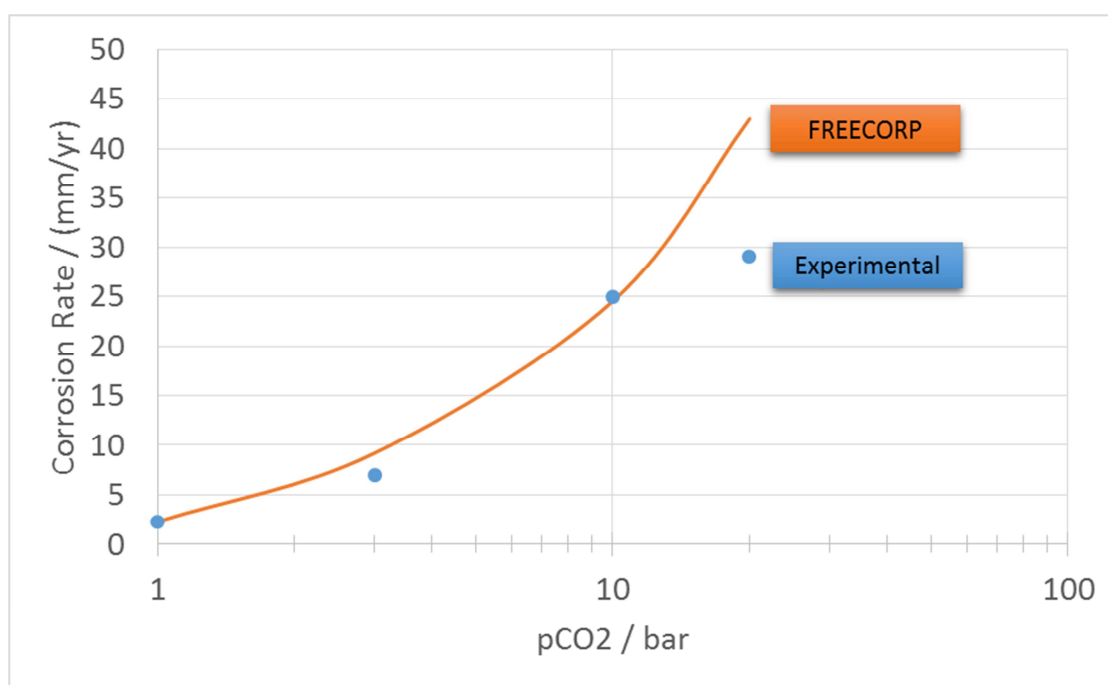


Figure 3: Comparison of model and experimental results at 60°C, pH 5, 1 m/s, 0.1 m ID single-phase pipe flow. Reproduced from FREECORP Background document [22].

This section serves as an introduction to FREECORP, and shows that the model works well at the conditions for which it was originally designed. However, when pushed to the upper limits of temperature and pressure, it begins to diverge from laboratory results. Since the conditions in production tubing are much more severe than

the conditions the model was calibrated for, it is clear that the model needs improvement in order to better predict downhole corrosion rates. The following sections will detail the improvements that have been added to FREECORP in the creation of WELLCORP.

In addition, FREECORP was designed as a point-model; that is, given one set of conditions, a point corrosion rate is calculated [10]. This model works well for predicting laboratory corrosion rates, and represents a single point in a line. In a real-world situation, however, corrosion at any given point in the tubing has an effect on corrosion of every point downstream, due to changing water chemistry and flow. That is to say, there is a sequence of points in a line with every point affecting the subsequent points, which was accounted for in WELLCORP.

## **4.2 WELLCORP**

The WELLCORP model was designed to predict corrosion rates for production tubing operating at high temperatures and pressures. As such, the point model, FREECORP, needed to be modified. This section will detail the important parameters, improvements added, program structure, and design of WELLCORP.

### **4.2.1 Input Parameters**

The following parameters are presented as required input data for the model:

- Flowing downhole and wellhead temperature.
- Flowing downhole and wellhead pressure.
- H<sub>2</sub>S and CO<sub>2</sub> content.

- Alkalinity.
- Total acetate concentration.
- Gas molecular weight.
- Production data: oil, gas, water mass flow rate.
- Internal Diameter (ID) of tubing.
- Length of production tubing.

The following parameters are optional inputs for the model:

- Complete brine composition.
- Complete gas composition.

#### 4.2.2 Output Parameters

The following parameters are presented as input data for the model:

- pH,  $\text{Fe}^{2+}$  concentration profile along the line.
- $\text{FeCO}_3$  saturation profile and precipitation rate along the line.
- $\text{CO}_2$  and  $\text{H}_2\text{S}$  fugacities along the line.
- Oil, gas, and water velocities along the line.
- Corrosion rate and scaling factor profile along the line.
- Cumulative wall thickness loss profile.

#### 4.2.3 Important Assumptions

The following assumptions are made in order to simplify the modeling work while maintaining the validity of the approach:

- The production tubing is a straight vertical line.
- There are no obstructions in the tubing, and its ID remains constant for the length of the line.
- Chemical inhibition is not taken into account.
- Supercritical fluids and corrosion are not taken into account, but calculation is prevented if the entire tubing string is above supercritical conditions.
- The tubing is assumed to be made of carbon steel.
- Ionic strength is assumed to be 0.1 M, unless a brine composition is provided.
- A linear temperature profile is assumed along the well depth.
- A linear pressure profile is assumed along the well depth.

#### 4.2.4 Equation of State

FREECORP assumes that the gas phase is ideal, but this is typically not a valid assumption for production tubing conditions. In order to account for non-idealities in the gas phase, a real-gas equation of state is required. This equation of state is used to calculate the compressibility factor and ultimately the fugacity, or effective pressure, of each gaseous species. WELLCORP implements the Peng-Robinson equation of state, Equation 18. It is a simple equation, yet offers a high accuracy for calculation of the compressibility factor at high temperatures and pressures for multi-component systems.

$$P = \frac{RT}{v - b} - \frac{a\alpha}{v(v + b) + b(v - b)} \quad (18)$$

Where:

$P$ : pressure, bar;

$R$ : universal gas constant with units, (L·bar)/(K·mol);

$T$ : absolute temperature, K;

$v$ : molar volume, L/mol;

$a$ : attraction parameter, (L<sup>2</sup>·bar)/mol<sup>2</sup>;

$b$ : van der Waals covolume, L/mol;

$\alpha$ : conversion factor for the attraction parameter between critical temperature and absolute temperature.

The attraction parameter and van der Waals covolume are both functions of critical temperature ( $T_c$ ) and pressure ( $P_c$ ).

The attraction parameter,  $a$ , is defined as:

$$a(T_c) = 0.45724 \frac{R^2 T_c^2}{P_c} \quad (19)$$

The van der Waals covolume,  $b$ , is defined as:

$$b(T_c) = 0.07780 \frac{RT_c}{P_c} \quad (20)$$

The conversion factor,  $\alpha$ , is defined as:

$$\alpha^{1/2} = 1 + \kappa \left(1 - T_r^{1/2}\right) \quad (21)$$

Where  $\kappa$  is a function of acentric factor,  $T_r$  is the reduce temperature and,  $\omega$  is defined as:

$$\kappa = 0.37464 + 1.54226\omega - 0.26992\omega^2 \quad (22)$$

Equation 18 can also be written in terms of compressibility factor,  $Z$ :

$$Z^3 - (1 - B)Z^2 + (A - 3B^2 - 2B)Z - (AB - B^2 - B^3) = 0 \quad (23)$$

$A$  in Equation 6 is defined as:

$$A = \frac{aP}{R^2T^2} \quad (24)$$

$B$  is defined as:

$$B = \frac{bP}{RT} \quad (25)$$

Finally,  $Z$  is defined as:

$$Z = \frac{Pv}{RT} \quad (26)$$

#### 4.2.5 Fugacity Coefficient

Fugacity coefficients are important parameters for high temperature and pressure applications. A fugacity coefficient is the ratio of the fugacity of a gas to its partial pressure. This allows a gas partial pressure to be converted to an effective gas pressure. Using the Peng-Robinson equation of state, shown above as Equation 18, fugacity coefficients can be calculated for each gaseous species, which provides a more accurate calculation of aqueous concentrations.

The fugacity coefficient ( $\Phi$ ) for a pure gas, as reported by Peng and Robinson, is shown in Equation 27:

$$\ln \frac{f}{p} = \ln \phi = Z - 1 - \ln(Z - B) - \frac{A}{2\sqrt{2}B} \ln \left( \frac{Z + 2.414B}{Z - 0.414B} \right) \quad (27)$$

Where:

$f$ : fugacity;

$p$ : partial pressure;

$Z$ : compressibility factor;

$A$ : defined by Equation 24;

$B$ : defined by Equation 25.

This equation is a simplified calculation of fugacity, as it assumes no interaction between gaseous species. Another form that does take interaction into account is shown in Equation 28. The binary interaction parameters ( $a_{ik}$ ) are found using Equation 29. The values for  $k_{ik}$  are taken from the literature [14, 15]. By using this form, a more accurate fugacity coefficient can be determined - one that takes into account the interaction of a species with the other species present.

$$\ln \frac{f_k}{x_k p} = \frac{b_k}{b} (Z - 1) - \ln(Z - B) - \frac{A}{2\sqrt{2}B} \left( \frac{2 \sum_i X_i a_{ik}}{a} - \frac{b_k}{b} \right) \ln \left( \frac{Z + 2.414B}{Z - 0.414B} \right) \quad (28)$$

$$a_{ik} = \sqrt{a_i a_k} (1 - k_{ik}) \quad (29)$$

Where:

$k$ : denotes the k-th component in the mixture;

$i$ : denotes the i-th component in the mixture;

$x$ : mole fraction;

$a_{ik}$ : binary interaction parameter;

$a$  and  $b$  are determined using the exact mixing rule [16].

#### 4.2.6 CO<sub>2</sub> Solubility

An improved CO<sub>2</sub> solubility model was implemented to extend the usable range of the line model. The new model is based on the semi-empirical Duan-Sun high temperature and high-pressure model [39]. The parameters for these equations are shown in Table 1, and the limits for this model are shown in Table 2. The procedure for calculating the molality of CO<sub>2</sub> in water and brine is shown in Equations 30-34.

$$\ln \frac{y_{CO_2} P}{m_{CO_2}} = \frac{\mu_{CO_2}}{RT} - \ln \varphi_{CO_2} + \ln \gamma_{CO_2} \quad (30)$$

Where:

$y_{CO_2}$ : Mole fraction of CO<sub>2</sub> in gas phase;

$P$ : Total pressure, bar;

$m_{CO_2}$ : Molality of CO<sub>2</sub> in liquid phase, mol/kg;

$\mu_{CO_2}$ : Chemical potential of CO<sub>2</sub>, J;

$R$ : Universal gas constant, J/mol·K;

$T$ : Absolute temperature, K;

$\varphi_{CO_2}$ : Fugacity of CO<sub>2</sub>;

$\gamma_{CO_2}$ : Activity coefficient of CO<sub>2</sub>.

$$\ln \gamma_{CO_2} = \sum_c 2\lambda_{CO_2-c} m_c + \sum_a 2\lambda_{CO_2-a} m_a + \sum_c \sum_a \xi_{CO_2-c-a} m_c m_a \quad (31)$$

Where:

$\lambda_{CO_2-c}$ : CO<sub>2</sub>-cation second-order interaction parameter (assumed 0);

$\lambda_{CO_2-a}$ : CO<sub>2</sub>-anion second-order interaction parameter (Equation 33);

$\xi_{CO_2-c-a}$ : CO<sub>2</sub>-anion-cation third-order interaction parameter (Equation 34);

$m_c$ : Molality of cation, mol/kg;

$m_a$ : Molality of anion, mol/kg.

$$\begin{aligned} \frac{\mu_{CO_2}}{RT} = & c_1 + c_2T + \frac{c_3}{T} + c_4T^2 + \frac{c_5}{630 - T} + c_6P + c_7P \ln T + \frac{c_8P}{T} \\ & + \frac{c_9P}{630 - T} + \frac{c_{10}P^2}{(630 - T)^2} \end{aligned} \quad (32)$$

$$\lambda_{CO_2-a} = c_1 + c_2T + \frac{c_3}{T} + \frac{c_8P}{T} + \frac{c_9P}{630 - T} + c_{11}T \ln P \quad (33)$$

$$\lambda_{CO_2-a-c} = c_1 + c_2T + \frac{c_3}{T} + \frac{c_8P}{T} + \frac{c_9P}{630 - T} \quad (34)$$

Where:

$T$ : Absolute temperature, K;

$P$ : Pressure, bar;

$c$ : T-P coefficient defined in Table 1.

Table 1: Interaction parameters for Duan-Sun CO<sub>2</sub> model [39]

<b>T-P coefficient</b>	$\mu_{\text{CO}_2}/RT$	$\lambda_{\text{CO}_2\text{-Na}}$	$\lambda_{\text{CO}_2\text{-Na-Cl}}$
c <sub>1</sub>	28.9447706	-0.411370585	3.36389723E-04
c <sub>2</sub>	-0.035458177	6.07632013E-04	-1.9829898E-05
c <sub>3</sub>	-4770.67077	97.5347708	
c <sub>4</sub>	1.02782768E-05		
c <sub>5</sub>	33.8126098		
c <sub>6</sub>	9.0403714E-03		
c <sub>7</sub>	-1.14934031E-03		
c <sub>8</sub>	-0.307405726	-0.023762247	2.1222083E-03
c <sub>9</sub>	-0.0907301486	0.0170656236	-5.248733303E-03
c <sub>10</sub>	9.32713393E-04		
c <sub>11</sub>		1.41335834E-05	

FREECORP uses the Odde-Tomson correlation for the CO<sub>2</sub> Henry's Law constant [40]. This Henry's Law constant correlation, however, does not cite any clear limits for the model. A comparison of the previous ideal model, Henry's Law, with the new semi-empirical model is shown in Figure 4. It shows quite clearly that the ideal model over predicts at high partial pressures of CO<sub>2</sub> when compared to the semi-empirical model. Therefore, the Duan-Sun model will provide more accurate CO<sub>2</sub> concentrations at high partial pressures, and thus improving the accuracy of the corrosion rate prediction. Duan and Sun clearly stated the limits of their solubility model, shown in Table 2. Additionally, they cite an uncertainty of 7% when compared with experimental values [39].

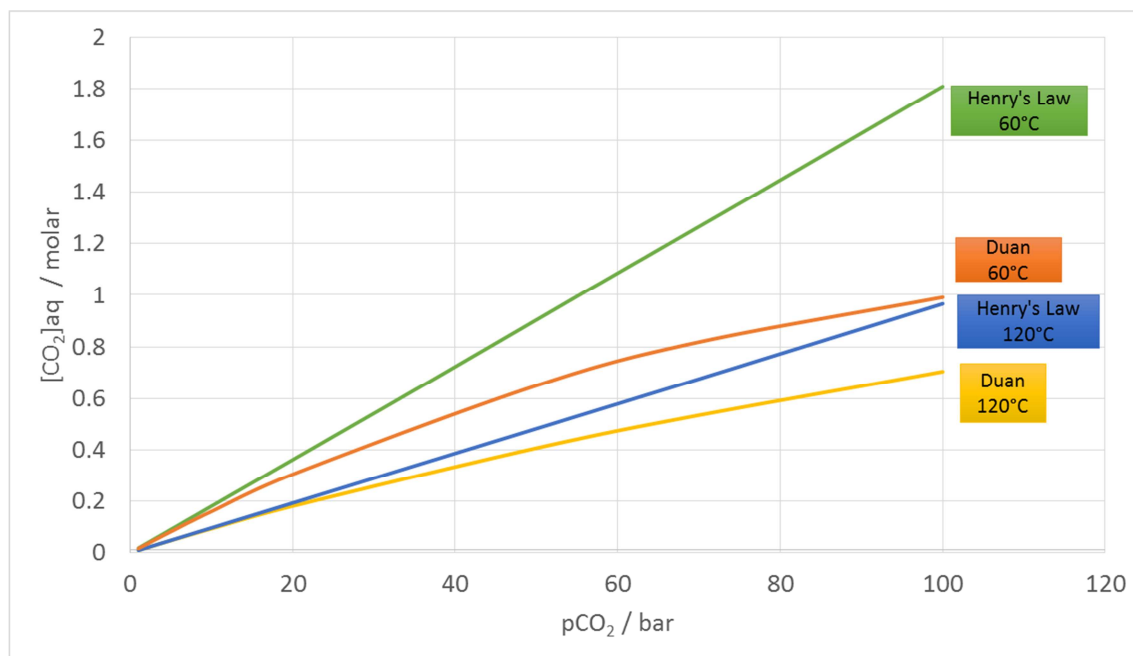


Figure 4: Comparison of Duan-Sun CO<sub>2</sub> solubility model with Henry's Law.

Table 2: Parameter limits for Duan-Sun CO<sub>2</sub> Solubility Model [39]

Parameter	Range
pCO <sub>2</sub>	1-2000 bar
Temperature	273 - 533 K
Ionic Strength	0 - 4.3 m

#### 4.2.7 H<sub>2</sub>S Solubility

Just as a new CO<sub>2</sub> solubility model is needed, so too is a new H<sub>2</sub>S solubility model. The semi-empirical model of Duan *et al.* was chosen for its large range of validity and also for its ability to account for salinity effects [41]. The procedure to calculate the molality of H<sub>2</sub>S in water is shown in Equations 35-39. The parameters for Equations 37-39 are shown in Table 3. The limits for this model are shown in Table 4.

$$\ln \frac{y_{H_2S}P}{m_{H_2S}} = \frac{\mu_{H_2S}}{RT} - \ln \phi_{H_2S} + \ln \gamma_{H_2S} \quad (35)$$

Where:

$y_{H_2S}$ : Mole fraction of H<sub>2</sub>S in gas phase;

$P$ : Total pressure, bar;

$m_{H_2S}$ : Molality of H<sub>2</sub>S in liquid phase, mol/kg;

$\mu_{H_2S}$ : Chemical potential of H<sub>2</sub>S, J;

$R$ : Universal gas constant, J/mol·K;

$T$ : Absolute temperature, K;

$\phi_{H_2S}$ : Fugacity of H<sub>2</sub>S;

$\gamma_{H_2S}$ : Activity coefficient of H<sub>2</sub>S.

$$\ln \gamma_{H_2S} = \sum_c 2\lambda_{H_2S-c}m_c + \sum_a 2\lambda_{H_2S-a}m_a + \sum_c \sum_a \xi_{H_2S-c-a}m_cm_a \quad (36)$$

Where:

$\lambda_{H_2S-c}$ : H<sub>2</sub>S-cation second-order interaction parameter (assumed 0);

$\lambda_{H_2S-a}$ : H<sub>2</sub>S-anion second-order interaction parameter (Equation 38);

$\xi_{H_2S-c-a}$ : H<sub>2</sub>S-anion-cation third-order interaction parameter (Equation 39);

$m_c$ : Molality of cation, mol/kg;

$m_a$ : Molality of anion, mol/kg.

$$\frac{\mu_{H_2S}}{RT} = c_1 + c_2T + \frac{c_3}{T} + c_4T^2 + \frac{c_5}{680 - T} + c_6P + \frac{c_7P}{680 - T} + \frac{c_8P^2}{T} \quad (37)$$

$$\lambda_{H_2S-a} = c_1 + c_2T + \frac{c_3}{T} + c_6P \quad (38)$$

$$\lambda_{H_2S-a-c} = c_1 \quad (39)$$

Where:

$T$ : Absolute temperature, K;

$P$ : Pressure, bar;

$c$ : T-P coefficient defined in Table 3.

Table 3: Interaction parameters for Duan *et al.* H<sub>2</sub>S model [41]

<b>T-P coefficient</b>	$\mu_{\text{H}_2\text{S}}/\text{RT}$	$\lambda_{\text{H}_2\text{S-Na}}$	$\lambda_{\text{H}_2\text{S-Na-Cl}}$
<b>c<sub>1</sub></b>	42.564957	8.5004999E-02	-1.08325890E-02
<b>c<sub>2</sub></b>	-8.6260377E-02	3.5330378E-05	
<b>c<sub>3</sub></b>	-6084.3775	-1.5882605	
<b>c<sub>4</sub></b>	6.8714437E-05		
<b>c<sub>5</sub></b>	-102.76849		
<b>c<sub>6</sub></b>	8.4482895E-04	1.1894926E-05	
<b>c<sub>7</sub></b>	-1.0590768		
<b>c<sub>8</sub></b>	3.5665902E-03		

Table 4: Parameter limits for Duan *et al.* H<sub>2</sub>S solubility model [41]

<b>Parameter</b>	<b>Range</b>
pH <sub>2</sub> S	1-200 bar
Temperature	273-500 K
Ionic Strength	0-6.0 m

FREECORP uses a correlation for H<sub>2</sub>S solubility based on IUPAC data [42]. It is similar to the CO<sub>2</sub> Henry's Law model in that it is a linear prediction. The H<sub>2</sub>S solubility model shows the same trend as the CO<sub>2</sub> solubility model - reduced solubility with increased partial pressure (Figure 5). The H<sub>2</sub>S model at 60°C shows a drastic decrease in solubility above 50 bar. This results in a 50 percent decrease in concentration at 100 bars of H<sub>2</sub>S compared to the ideal model.

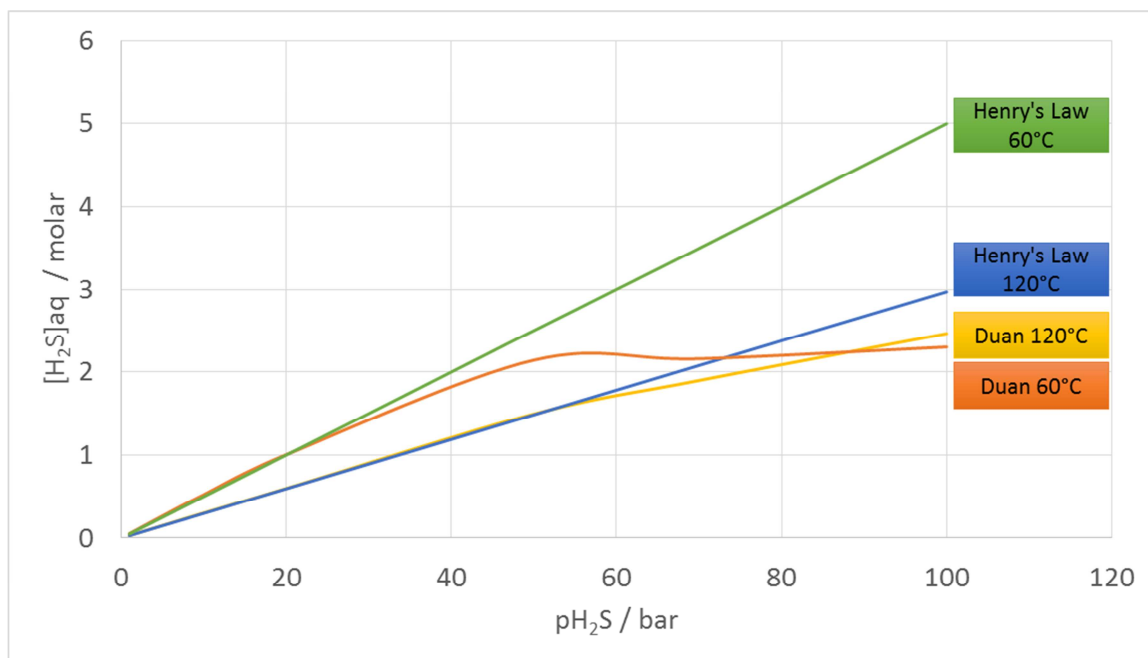


Figure 5: Comparison of Duan *et al.* H<sub>2</sub>S solubility model with Henry's Law.

#### 4.2.8 Activity Coefficient

The activity of a species can be thought of as the effective concentration in solution. This is similar to fugacity representing the effective partial pressure of a gas. As species are introduced to the aqueous phase, the molecules will interact with other molecules when at high concentrations. This can result in a lower or higher activity depending on the species present.

WELLCORP implements the Pitzer activity model to account for the electrostatic forces [34], [35]. His model is based on the theoretical work of Debye and Hückel. However Pitzer, in order to extend the validity range, extended the model by fitting several parameters of a virial expansion of the equation for Gibb's free energy. The resulting equation for the Pitzer activity coefficient is shown below.

$$\ln \gamma = |z_M z_X| f^\gamma + m \left( \frac{2v_M v_X}{v} \right) B_{MX}^\gamma + m^2 \frac{2(v_M v_X)^{3/2}}{v} \left( \frac{3}{2} \right) C_{MX}^\varphi \quad (40)$$

Where:

$\gamma$ : Activity coefficient;

$z_M$ : Charge of species M;

$z_X$ : Charge of species X;

$f^\gamma$ : Defined in Equation 41;

$m$ : Molality, mol/kg solvent;

$v_M$ : Number of M ions in the formula;

$v_X$ : Number of X ions in the formula;

$v$ : Sum of  $v_M$  and  $v_X$ ;

$B_{MX}$ : Defined in Equation 42;

$C_{MX}$ : Defined in Table 5;

$f^\gamma$  is defined as:

$$f^\gamma = -A_\varphi \left[ \frac{I^{1/2}}{1 + bI^{1/2}} + \frac{2}{b} \ln(1 + bI^{1/2}) \right] \quad (41)$$

Where:

$A_\varphi$ : Debye-Hückel coefficient;

$b$ : Constant equal to 1.2;

$I$ : Ionic strength, mol/kg.

$$B_{MX}^\gamma = 2\beta_{MX}^{(0)} + \frac{2\beta_{MX}^{(1)}}{\alpha^2 I} \left[ 1 - e^{-\alpha I^{1/2}} \left( 1 + \alpha I^{1/2} - \frac{1}{2} \alpha^2 I \right) \right] \quad (42)$$

Where:

$\alpha$ : Constant equal to 2.0;

$\beta_{MX}^{(0)}$ : Constant dependent on the electrolyte (Table 5);

$\beta_{MX}^{(1)}$ : Constant dependent on the electrolyte (Table 5);

$I$ : Ionic strength, mol/kg.

Table 5: Electrolyte parameters for Pitzer activity model

Species	$\beta^{(0)}$	$\beta^{(1)}$	$C^\phi$
HCl	0.1775	0.2945	0.0008
NaCl	0.0765	0.2664	0.00127
KCl	0.04935	0.2122	-0.00084
NaOH	0.0864	0.253	0.0044

The original Debye-Hückel model assumed that all species of similar charge would have the same activity. In addition, the ionic strength limit of the original model was 0.2 m, much smaller than the Pitzer model. In the range of 0-0.2 m ionic strength, the assumption is true. This can be seen in Figure 6. The first part of the curves, below  $I^{1/2} = .5$ , are similar for all three curves. However, above this, the Pitzer model predicts very different activity coefficients for each species. In the case of the bicarbonate ion ( $\text{HCO}_3^-$ ) the activity of hydrogen ions protons ( $\text{H}^+$ ), and similarly for hydroxide ( $\text{OH}^-$ ), rises with increasing ionic strength.

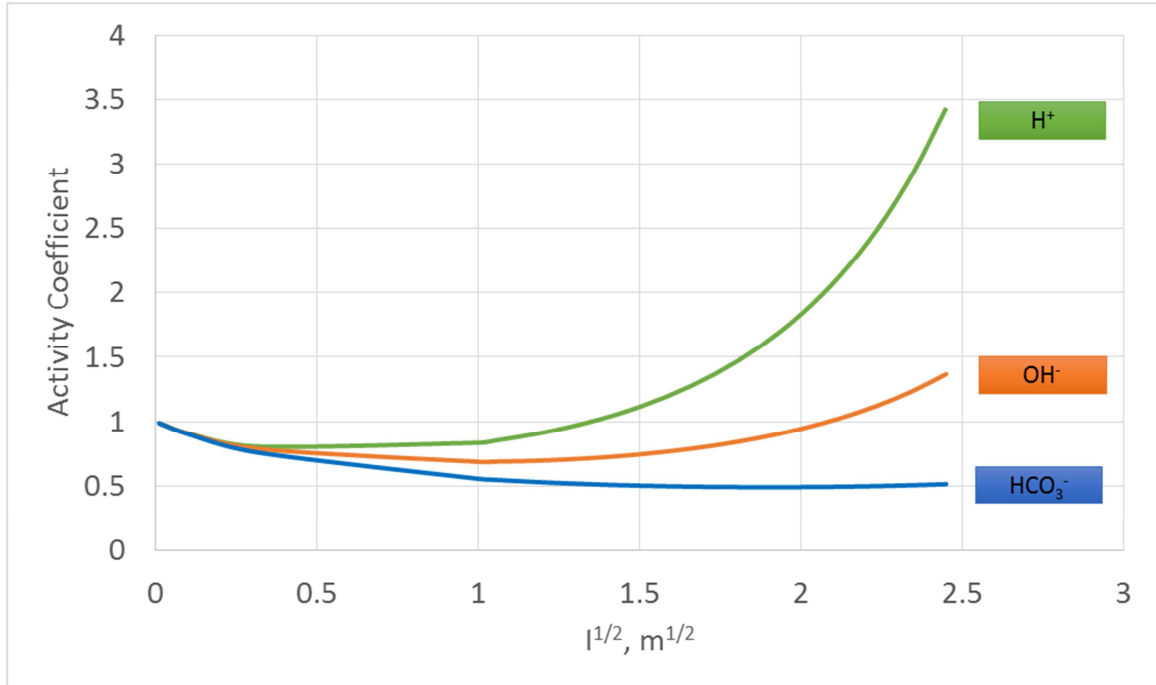


Figure 6: Comparison of Pitzer activities for  $H^+$ ,  $OH^-$ , and  $HCO_3^-$ .

#### 4.2.9 Ferrous ( $Fe^{2+}$ ) Ion Concentration Calculation

The  $Fe^{2+}$  concentration is an important input parameter for the corrosion calculation as it controls the saturation value of  $FeCO_3$ , the  $FeCO_3$  precipitation rate and the value of the  $FeCO_3$  scale factor. It can be calculated at every step along the line by considering a mole balance of  $Fe^{2+}$  (balance between inlet/outlet fluxes, corrosion, and precipitation) as shown in Equation 43. Iterations are computed for each segment of pipe until convergence is achieved with regard to the  $Fe^{2+}$  concentration. The corresponding corrosion rate is then displayed.

$$c_{Fe_{out}^{2+}} = c_{Fe_{in}^{2+}} + \frac{((CR - PR) * \rho_{Fe} * A_p)}{(M_{Fe} * A_c * v)} \quad (43)$$

Where:

$c_{Fe_{out}^{2+}}$ : Concentration of  $Fe^{2+}$  exiting the control volume,  $mol/m^3$ ;

$c_{Fe_{in}^{2+}}$ : Concentration of  $Fe^{2+}$  entering the control volume,  $mol/m^3$ ;

$CR$ : Average corrosion rate at the control volume,  $m/yr$ ;

$PR$ : Precipitation rate,  $m/yr$ ;

$\rho_{Fe}$ : Density of iron,  $kg/m^3$ ;

$A_p$ : Surface area of pipe,  $m^2$ ;

$M_{Fe}$ : Molecular mass of iron,  $mol/m^3$ ;

$A_c$ : Cross-section area of pipe,  $m^2$ ;

$v$ : Velocity of fluid,  $m/s$ .

#### 4.2.10 Water Condensation Rate Calculation

In most cases, a significant amount of water is produced through the well. This water can come from condensation of the water vapor and from formation water. The rate of water drop out from condensation can be calculated based on the temperature and pressure profiles. If the calculated rate of water drop out is larger than the total water flow rate measured at the wellhead, it is then assumed that the gas stream was not always saturated with water vapor. This means that some sections of the tubing downstream of the bottom hole may have been dry (no liquid water present and consequently no corrosion).

The saturation water vapor pressure is calculated as follows [10]:

$$P_s = \exp\left(\frac{a + bt}{236 + t}\right) \quad (44)$$

Where:

$$a = 1514 \text{ and } b = 23.59;$$

$t$ : Temperature, °C;

$P$ : Saturation pressure, Pa.

Usually a chart, such as the one shown in Figure 7, is read manually by the engineer or technician to obtain the water content of natural gas, but there are many correlations available for these water content charts [43]. From the long list of correlations, the following equation was picked for its simplicity and wide temperature and pressure validity range (up to 10,000 psi and 460°F):

$$W = 47484 \frac{P_{sat}}{P_t} + B \quad (45)$$

B is calculated as:

$$B = \frac{-3083.87}{459.6 + T} + 6.69449 \quad (46)$$

Where:

$W$ : Water content, lb/MMCF;

$P_{sat}$ : Saturation pressure define in Equation 44, Pa;

$P_t$ : Total pressure, Pa;

$B$ : Temperature correction factor;

$T$ : Temperature, °F.

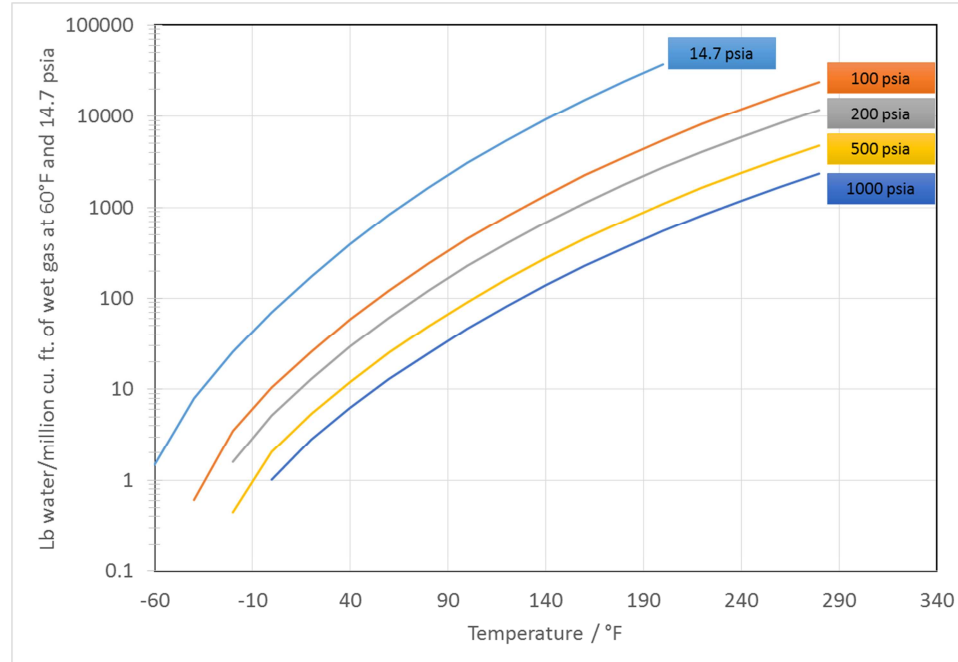


Figure 7: Water content of natural gas. Produced with the Bukacek correlation [43].

Equation 45 has limits, however. It can only predict the water content of sweet natural gas that contains low concentrations of  $\text{CO}_2$  and  $\text{H}_2\text{S}$  [43]. If  $\text{H}_2\text{S}$  is present in high concentrations the equation no longer makes accurate predictions, but is still an improvement over the ideal gas method.

The water dropout rate can be calculated according to the following scheme:

1. Calculate the total water dropout from condensation (WCR) in the well from bottom to top.
2. Compare WCR to the water production rate ( $Q_w$ ) measured at the well head:
  - a. If  $Q_w > \text{WCR}$ , this implies that formation water is produced and that liquid water is always present from the bottom,

- b. If  $Q_w < WCR$ , this implies that no formation water is produced, and that liquid water is not present along the entire length of the tubing (at least at the beginning). The location where the water vapor starts condensing is back-calculated from the point where  $WCR$  becomes equal to  $Q_w$ . Upstream of the point, the corrosion rate is considered zero.

3. The water film velocity is calculated and serves as an input for the point model.

#### 4.2.11 Flow Model

FREECORP currently does not have a flow model. It instead assumes full liquid pipe flow. Therefore, the superficial velocity corresponds to the in situ velocity. This assumption does not work for multiphase oil and gas wells, where there are often two or three phases present. The multiphase flow model used in WELLCORP stems from the work of Jauseau [44]. The original model is capable of predicting flow patterns and velocities for a wide variety of conditions, including horizontal and vertical flow. To simplify the prediction calculation, the production tubing is assumed to be vertical. WELLCORP, by default, also assumes a flow regime, rather than predicting one, which simplifies and speeds up the calculation process. These simplifications make the calculation significantly faster, but the option to run the full model to predict the flow regime is available in the single-day-run model of WELLCORP and is not available in the production data analysis module.

Each flow regime requires a different set of calculations to arrive at in situ velocities. All the algorithms require the calculation of Reynolds numbers, friction

factors, and shear stress. Finally, the momentum balance must be solved using an iterative scheme to return the in situ velocities.

Once the flow model has returned the in-situ phase velocities, the only parameter used in the corrosion calculation is water velocity. FREECORP uses water velocity to calculate an empirical flow factor for carbonic acid reduction, and for mass transfer coefficient calculations for other reducible species [10]. The flow factor has an effect on the CO<sub>2</sub> hydration reaction, and thus is present in the limiting current calculation for carbonic acid (Equation 47).

$$i_{lim,H_2CO_3} = F c_{CO_2} (\eta_{FeCO_3} \eta_{FeS} D_{H_2CO_3} K_{hyd} k_{hyd}^f)^{0.5} f \quad (47)$$

Where:

$c_{CO_2}$ : Concentration of CO<sub>2</sub> in the bulk solution, mol/m<sup>3</sup>;

$\eta_{FeCO_3}$ ,  $\eta_{FeS}$ : Scale factors for FeCO<sub>3</sub> and FeS respectively;

$D_{H_2CO_3}$ : Diffusion coefficient of carbonic acid in water, m<sup>2</sup>/s;

$K_{hyd}$ : Equilibrium constant for carbon dioxide hydration reaction;

$k_{hyd}^f$ : Forward reaction rate constant for carbon dioxide hydration reaction;

$f$ : Flow factor affecting carbon dioxide hydration.

#### 4.2.12 Material Guidance

In production tubing, failures often occur due to a combination of corrosion and cracking [45]. The NACE MR0175 standard provides guidance for steel selection used in sour applications [30]. This standard breaks conditions into four zones based on the likelihood that sulfide stress cracking (SSC) will occur; they are defined by pH and H<sub>2</sub>S partial pressure ranges. Figure 8 shows the distribution of SSC risk zones. As the zone

number increases, the risk of SSC increases and the more stringent the standard. For example, if conditions fall in the SSC zone 1, the standard calls for a steel with a maximum Rockwell Hardness on the C scale (RHC) of 30, and an actual yield strength (AYS) of less than 130 ksi.

Currently this feature is not implemented in WELLCORP, but a spreadsheet was created to calculate the SSC zone for a given pH and partial pressure of H<sub>2</sub>S. It can easily be integrated, and will be added to future work.

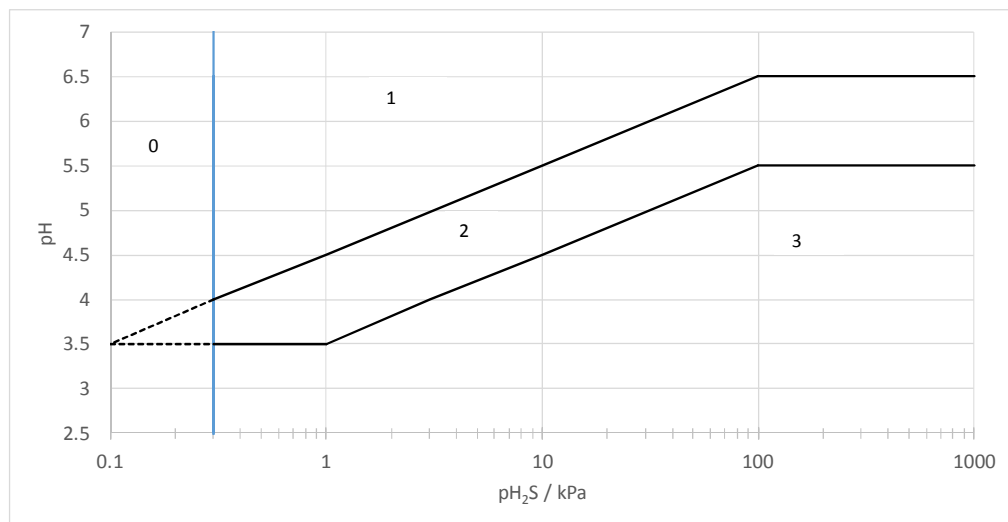


Figure 8: NACE MR0175 SSC zone map. Adapted from NACE MR0175 standard [30].

### 4.3 Program Design and Structure

#### 4.3.1 Line Model

##### 4.3.1.1 Algorithm

WELLCORP was designed to be a line model. A line model is essentially a series of linked point models (Figure 9). Each point model is calculated at a different set of

conditions. The main factors linking the individual point models are pH and  $\text{Fe}^{2+}$  concentration. The iron produced in the bottommost point will flow up the pipe and affect the following points.

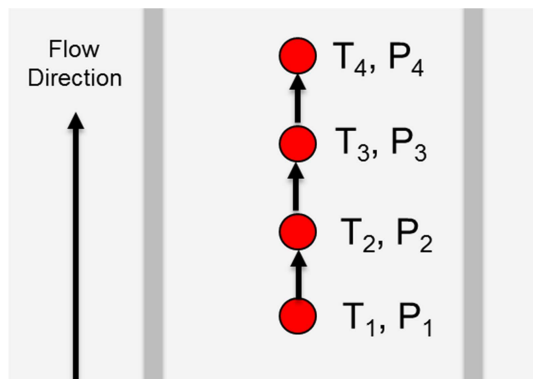


Figure 9: Schematic of a line model

WELLCORP is divided into two separate modules—a single day run, and production data analysis. The main calculation algorithm is identical for the two modules (Figure 10). However, the overall calculation processes are slightly different. The calculation starts by finding the total amount of water dropout in the tubing section using the water content difference between the bottom and top of the section. The superficial velocities are calculated and passed to the flow model to determine in situ velocities. Three pH values are calculated using three different values of  $\text{Fe}^{2+}$  concentration (initially 0, 500, and 1000 ppm), along with alkalinity, HAc acid concentration, carbonic species, and sulfide species concentrations. Three point models are calculated using the three different pH and  $\text{Fe}^{2+}$  concentration values. The iron mass balance is calculated for each point model. The  $\text{Fe}^{2+}$  concentrations are updated depending on the results of the mass

balance check. This process continues until a corrosion-precipitation rate balance is found. The final step is to calculate the corrosion product stability with an algorithm similar to ThermoCORP (described below).

The production data analysis module has fewer inputs, but allows for the input of multiple days of production data. Output is a plot of cumulative wall loss at each depth, as well as numerical output of important parameters such as corrosion rate and pH. The single day run allows for a more comprehensive set of inputs, such as detailed brine and gas compositions, but does not take into account time.

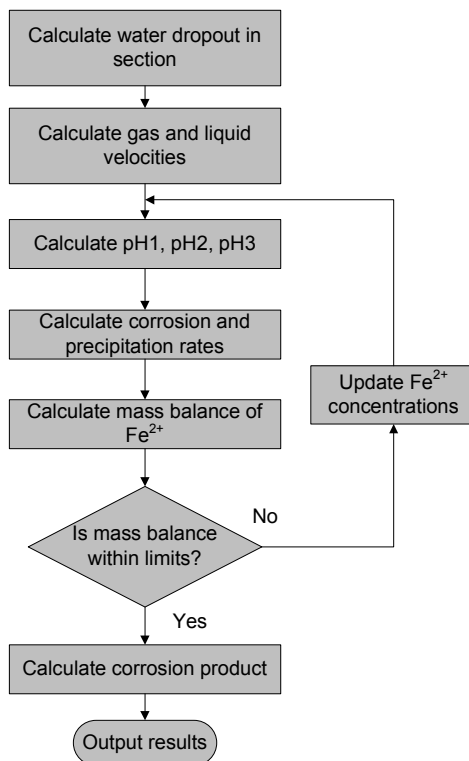


Figure 10: WELLCORP main calculation algorithm

#### 4.3.1.2 Program Architecture

WELLCORP is programmed in an object-oriented manner. The program consists of following three main modules: input, calculation, and output. It can be more specifically broken into seven classes and a graphical user interface (GUI.) These classes are listed and described in Table 6. The structure of WELLCORP is shown in Figure 11. The public methods for each class are shown in Table 7 - Table 10. The methods of the AnodicReaction and CathodicReaction classes have similar names and functions. The Brine and Gas classes have no public methods, as they are used for storage and automated calculations. The GUI and the program are separated, allowing for easy integration into future applications. The input module loads the model, sets the default values, and validates user data. Additionally, the input module vacillates the setting and retrieval of data to and from the calculation module. After the calculation is completed, the output module displays the results on the results plot, as well as onto an Excel spreadsheet.

Table 6: WELLCORP class description

<b>Class</b>	<b>Description</b>
LineModel	Handles point linkage and conditional changes along the line
PointModel	Calculates corrosion rate for a single set of conditions
AnodicReaction	Calculates the anodic reaction parameters
CathodicReaction	Calculates the cathodic parameters
Brine	Stores and calculates brine parameters
Gas	Stores and calculates gas parameters
FlowModel	Calculates flow regime and phase velocities

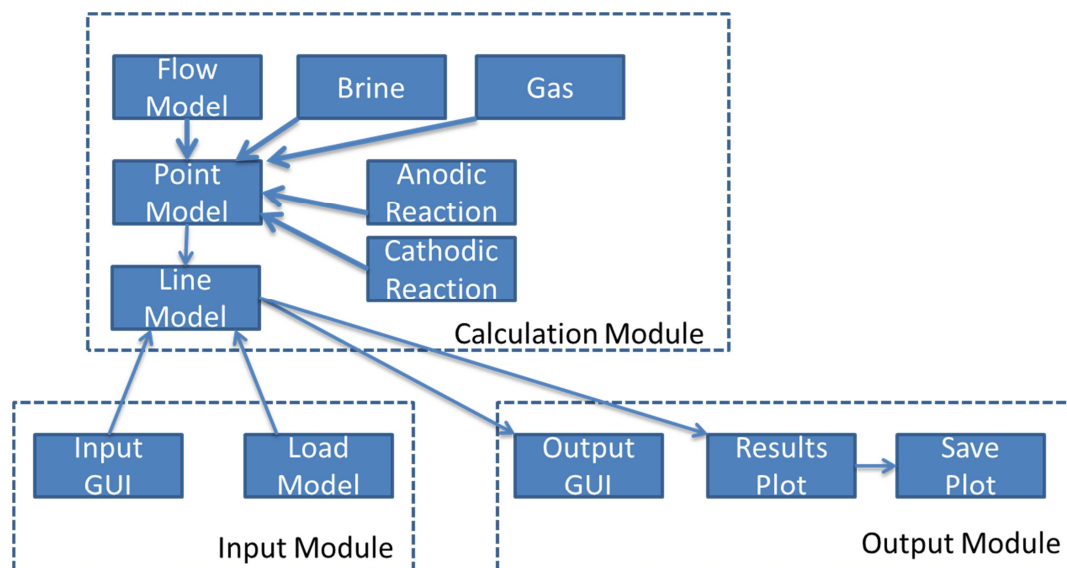


Figure 11: WELLCORP program structure

Table 7: Public methods of the LineModel class

Method	Description
Initialize	Sets default values and initializes array parameters
CalcCR	Main subroutine for calculating all major outputs (i.e. corrosion rate, pH, iron concentration, etc.)
getPsatWater	Returns the partial pressure of water vapor
getFugacity	Returns the fugacity for a single gas species
getWaterDropout	Returns the water content difference between downhole and wellhead conditions
getMixedFugacity	Returns the fugacity for a mixture of gases
getConcCO2Duan	Returns the aqueous concentration of CO <sub>2</sub> using the Duan model
getConcH2SDuan	Returns the aqueous concentration of H <sub>2</sub> S using the Duan model
PitzerActivity	Returns the activity coefficient for an aqueous species

Table 8: Public methods of the PointModel class

Method	Description
Initialize	Initializes and calculates shared variables
getCR	Returns the overall corrosion rate
CalcCO2CorrosionRate	Calculates the CO <sub>2</sub> corrosion rate
CalcCorpot	Calculates the corrosion potential

Table 9: Public methods of the AnodicReaction and CathodicReaction classes

<b>Method</b>	<b>Description</b>
Intialize	Initializes and calculates shared variables
getCurrentDensity	Returns the current density at a given potential
getCurrentDensityArray	Returns an array of current density for a range of potentials

Table 10: Public methods of the FlowModel class

<b>Method</b>	<b>Description</b>
Intialize	Initializes and calculates shared variables
Calculate	Main subroutine to determine flow pattern and phase velocities
FLOPAT_AnnularMist	Calculates phase velocities for annular mist flow regime
FLOPAT_SLug	Calculates phase velocities for intermittent slug flow regime
Transition_AM_IN	Determines if the flow pattern is annular mist or intermittent slug

### 4.3.2 Single Day Run

#### 4.3.2.1 Algorithm

The single day run is designed to analyze a single set of production data. Before the program can run, the data is validated to ensure that it is within the limits of the model. A visual representation of this algorithm is shown in Figure 12. The calculation starts by computing the total water dropout and ascertains whether water is present. If not the point is skipped. Next, the calculation goes into the main algorithm discussed above. This process continues along the length of the tubing at each depth until the wellhead is reached. Finally, the results are exported to the interface, as well as an Excel spreadsheet.

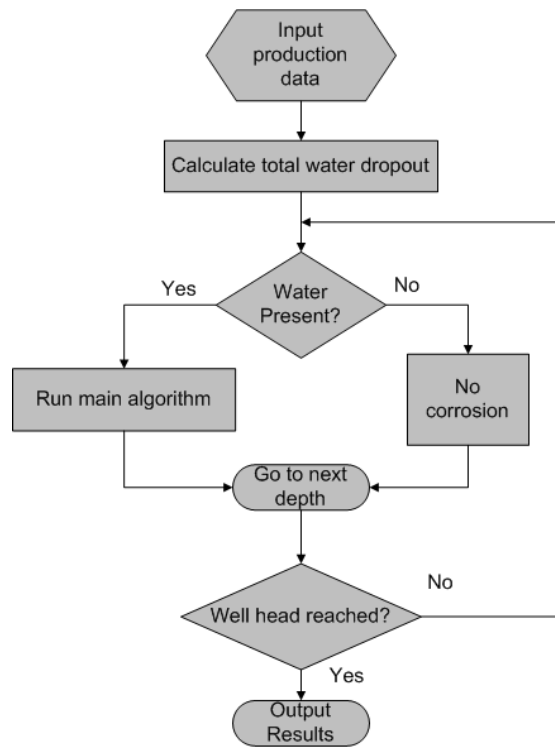


Figure 12: Schematic of single day run algorithm.

#### 4.3.2.2 Graphical User Interface

The interface for this portion of the program was designed to facilitate quick input and analysis of a single day of production data (shown in Figure 13). In addition to the main window there are also advanced input windows. They are as follows: gas composition input (Figure 14), brine composition input (Figure 15), and flow model input (Figure 16).

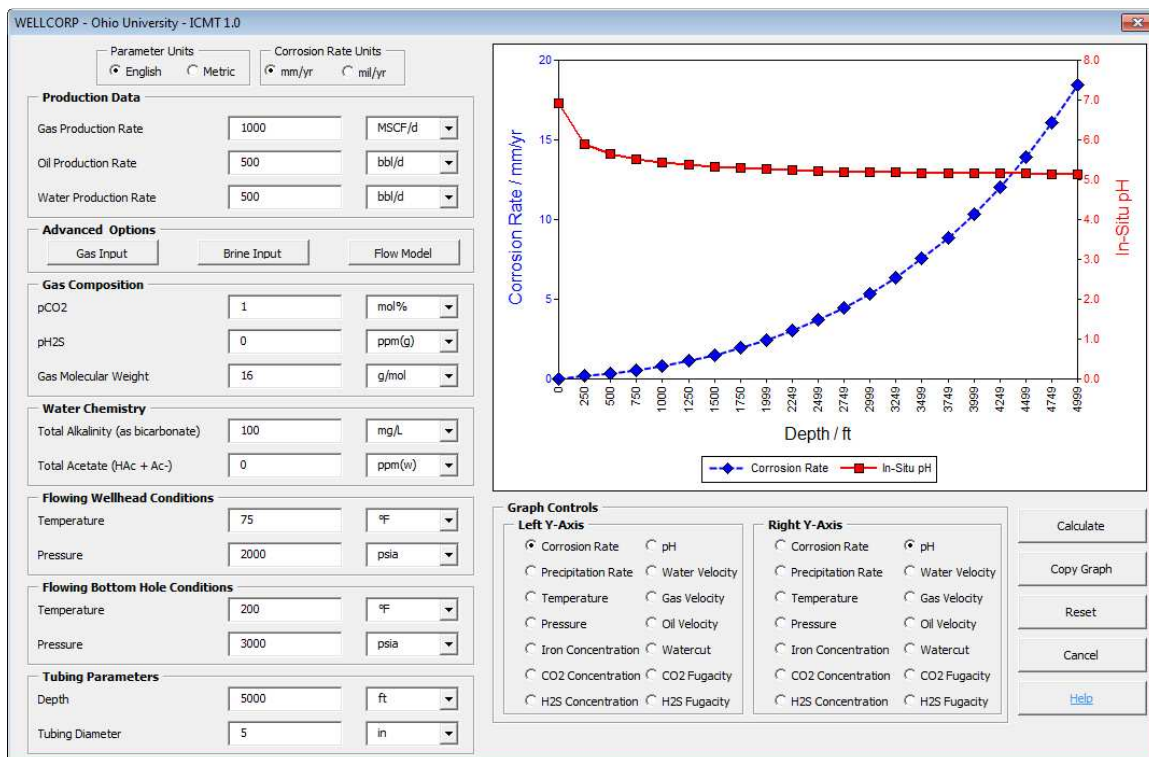


Figure 13: WELLCORP interface

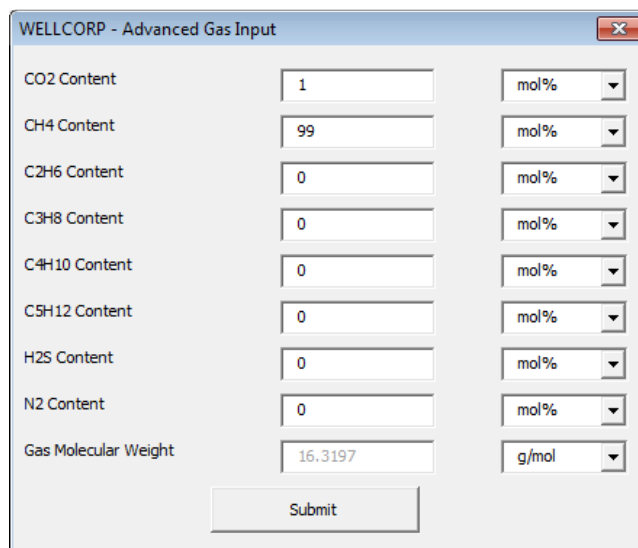


Figure 14: Advanced gas input window

WELLCORP - Advanced Brine Input

Alkalinity (HCO <sub>3</sub> <sup>-</sup> )	100	mg/L
Acetate (HAc + Ac <sup>-</sup> )	0	ppm(w)
Cl <sup>-</sup>	10000	ppm(w)
Na <sup>+</sup>	0	ppm(w)
K <sup>+</sup>	0	ppm(w)
Ca <sup>2+</sup>	0	ppm(w)
Mg <sup>2+</sup>	0	ppm(w)
Ionic Strength	0.142	M

Submit

Figure 15: Advanced brine input window

WELLCORP - Flow Model Options

Choose Model

Predict Flow Regime     Assume Flow Regime

Choose Flow Assumption

Intermittent     Annular

This option only considers the intermittent flow regime. It provides faster calculation times than the full model.

Submit

Figure 16: Flow model input window

### 4.3.3 Production Data Analysis

#### 4.3.3.1 Algorithm

The algorithm for the production data analysis module is similar to that of the single day run with a few exceptions. It must loop over multiple sets of inputs and there are few input options. The program calculates the output parameters with depth for one day of production before moving to the next set of production data. Once the data for the final day of production is calculated, the cumulative wall loss is calculated and plotted. A schematic of this algorithm is shown in Figure 17.

In calculating the cumulative wall loss, the program assumes the corrosion is constant between non-consecutive days. That is, if production data is input on the first of each month, the corrosion rate calculated on the first day is assumed to occur every day until the next day of production data.

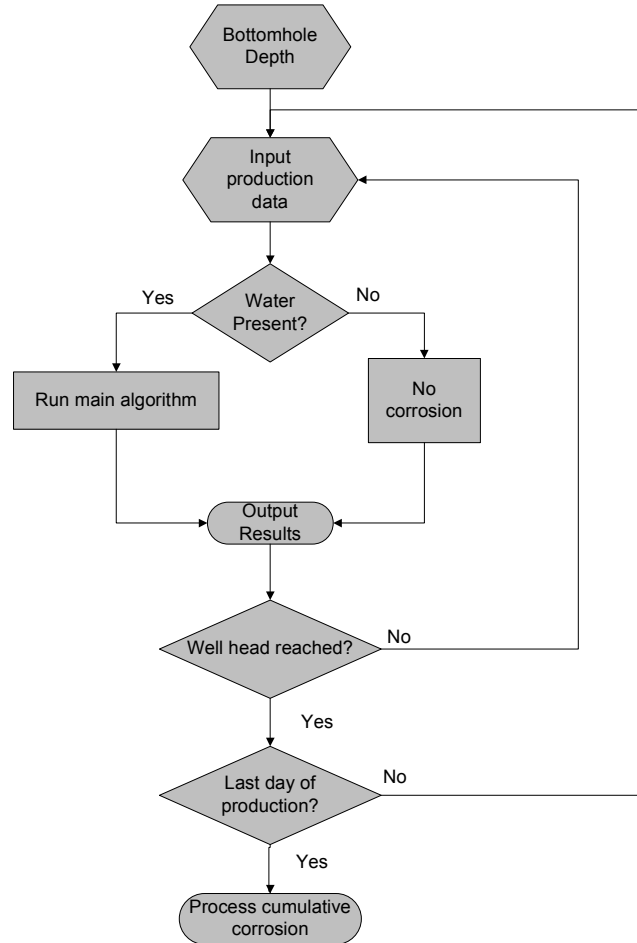


Figure 17: Schematic of production data analysis algorithm

#### 4.3.3.2 Graphical User Interface

The input and output for this module is facilitated through an Excel spreadsheet template. This template is generated, and the user inputs the production data for at least two days of production. The calculation may be started and the template is generated through the window shown in Figure 18. After the calculation is finished, a plot of cumulative wall loss with depth is generated (Figure 19).

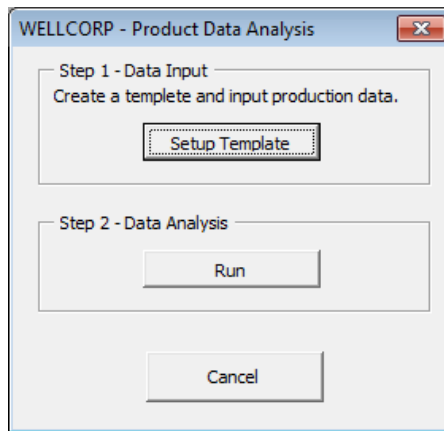


Figure 18: Interface for WELLCORP production data analysis

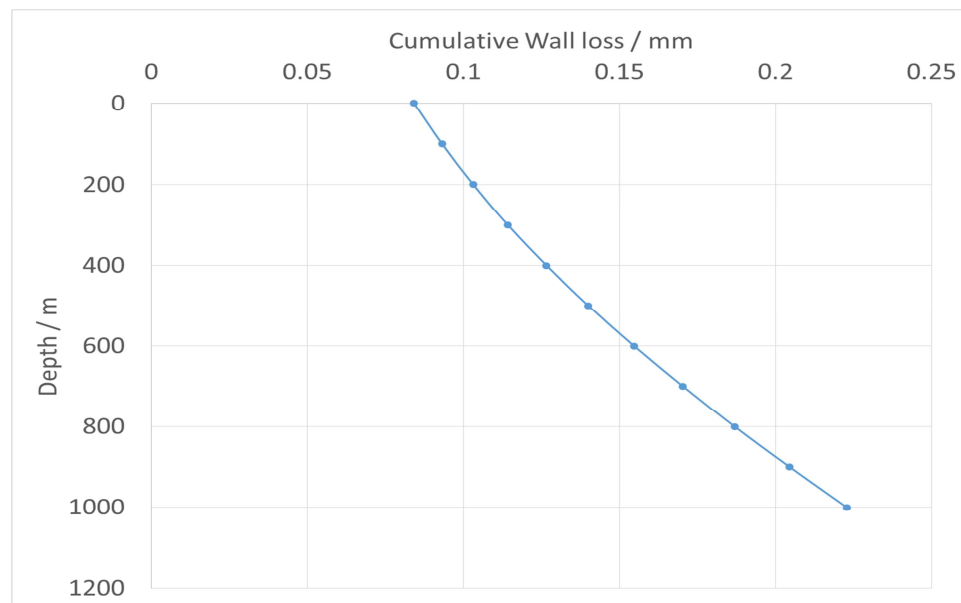


Figure 19: Example of data analysis production cumulative wall loss result

## 4.4 Results and Discussion

### 4.4.1 FREECORP Improvements

As discussed in previous sections, many modifications were made to FREECORP to improve corrosion rate predictions. Main among these was the improvement over Henry's Law. This change, combined with the addition of activity and fugacity coefficients, improved corrosion predictions at high partial pressures of CO<sub>2</sub>.

The model comparisons at 3, 10, and 20 bar CO<sub>2</sub> are shown in Figure 20. In all cases, the WELLCORP point model outperformed the original FREECORP model and yielded results similar to that of MULTICORP. The model still over-predicted the corrosion rate, but by a smaller margin than FREECORP. This reduction in corrosion rate will yield lower wall loss predictions when used with the line model. Error bars represent the maximum and minimum measurement corrosion rates.

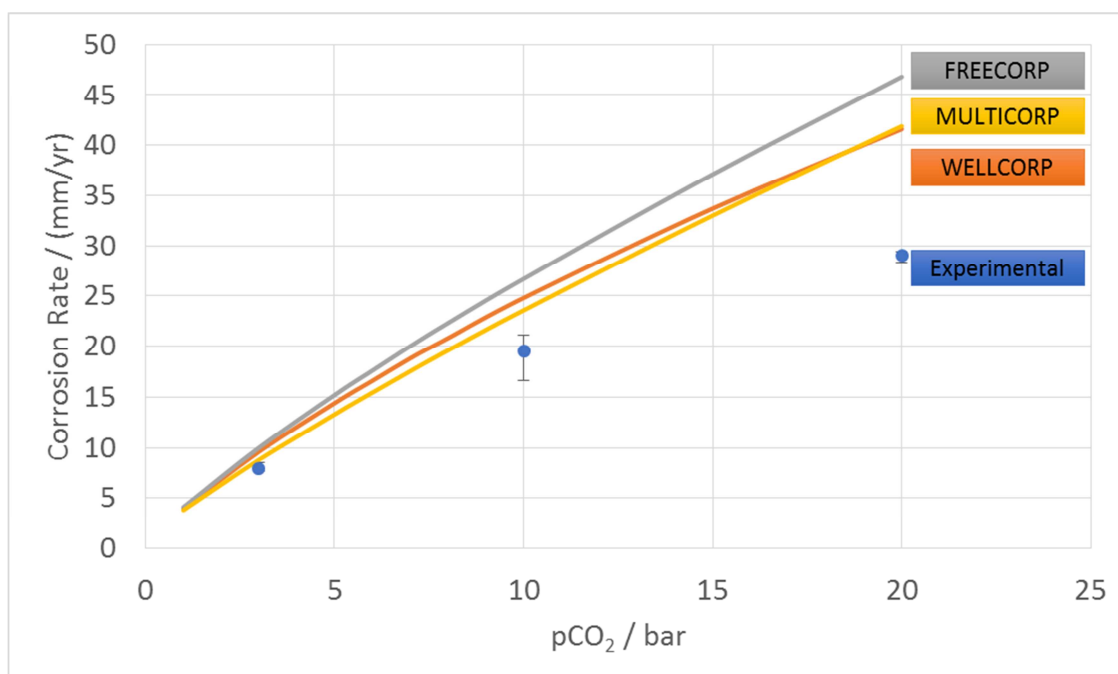


Figure 20: Comparison between corrosion models and experimental data, at 60°C, pH 5.0, 1 m/s, 1 wt% NaCl. Experimental data take from Wang *et al.* [21].

The results at 80 bar CO<sub>2</sub> (Figure 21) showed a greater improvement than the previous results at lower partial pressures. The over-prediction at these conditions was reduced by nearly 40 percent. The WELLCORP point model predicted the lowest corrosion rate of all the models tested. Similar to the previous comparison, this reduction in corrosion rate will reduce the predicted wall losses by the line model. Error bars represent the maximum and minimum measurement corrosion rates.

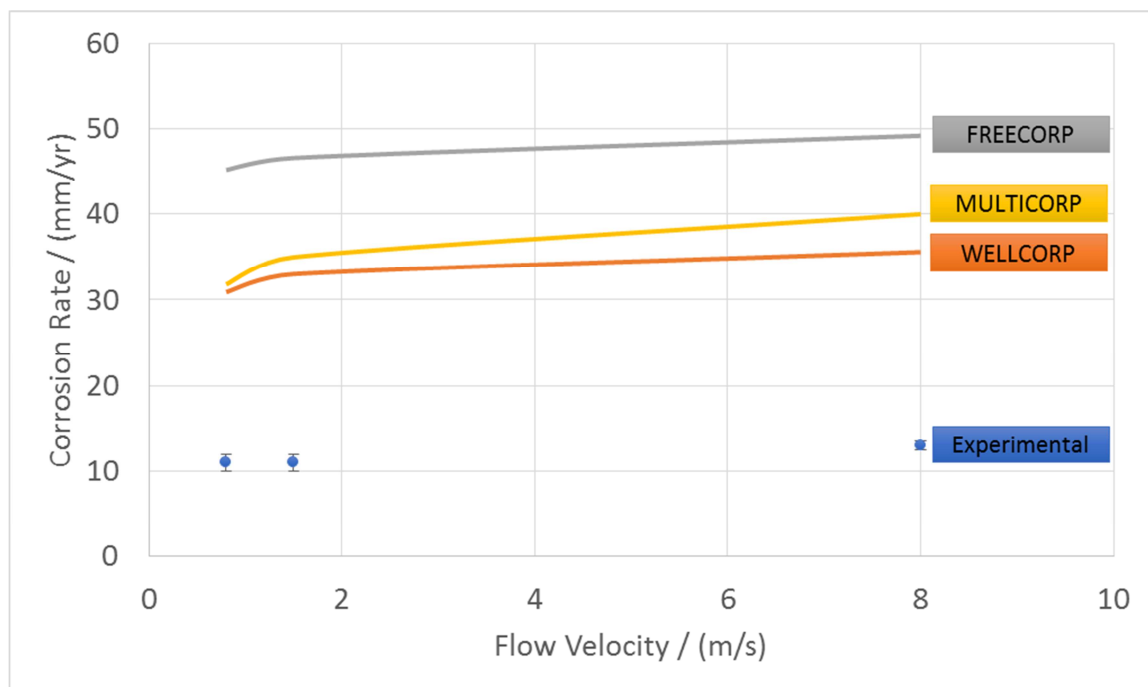


Figure 21: Comparison between corrosion models and experimental data, at 80 bar CO<sub>2</sub>, 25°C, pH 3.0, 1 m/s, 1 wt% NaCl. Experimental data take from Nor *et al.* [46].

#### 4.4.2 Analysis of Field Data

Two important sets of data were provided by the sponsor. The first set of data is the production data on which the simulations will be run. The second set of data is the caliper data, to which the simulations will be compared. All the data provided comes from the same field, as such the wells are expected to have similar compositions. The wells are drilled at different depths, so bottom-hole temperatures and pressures will be different for each well. Note that all results have been normalized for confidentiality reasons. This was achieved by multiplying all wall losses, measured and calculated, by a constant factor.

As mentioned in the literature review, field data is often sporadically measured. Exacerbating this challenge is the tendency for a field to change operators several times

over its lifetime, so data can be lost or not provided to the new owner. This set of data is not exempt from these problems. Some of the wells have production data reported in the 1980s, but temperature and pressure data is not reported until the 1990s or 2000s. From the amount of data provided, only four wells have enough data to simulate accurately.

Some important assumptions were made about these data, first, that the wells operated continuously. Second, if data were missing, the last reported point was assumed until the next data point. Only a few fields report H<sub>2</sub>S concentrations, but since the wells are all in the same field, this concentration of H<sub>2</sub>S was assumed for all wells.

The caliper data had to be processed before data could be plotted. Each well had several million data points for each caliper run. Caliper data at each depth were averaged, and were then periodically sampled to get the final set. Each well had different wall loss trends according to the caliper data. The normalized caliper data for each well is shown in Figure 22 - Figure 25.

Well A shows a large degree of negative wall loss, or wall gain, near the reservoir. This is likely due to scaling, as meetings with the sponsor revealed that scaling was an issue in other wells in this field. The overall trend for Well B is an increase of wall loss with depth. This is expected, since the partial pressure of acid gases is the highest at the reservoir inlet. The trend of Well C is relatively flat, with high wall loss at the wellhead. Well D shows a wavy trend. The bottom half of the tubing largely shows wall gains from scaling and the top half of the tubing show wall loss.

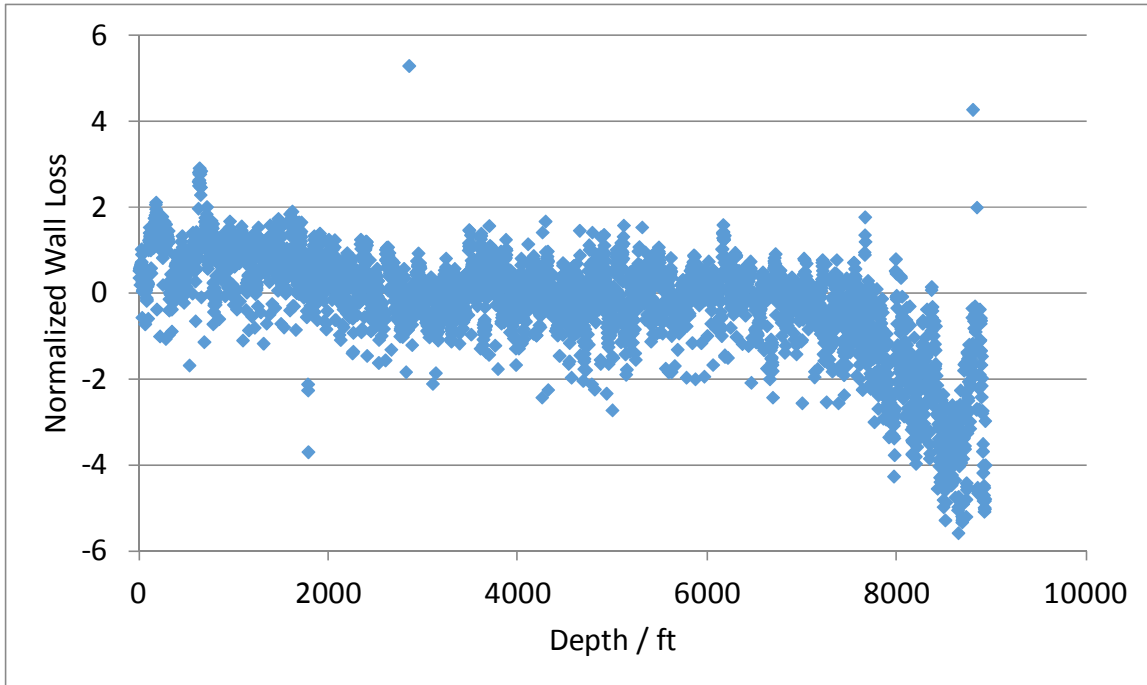


Figure 22: Normalized caliper data for Well A

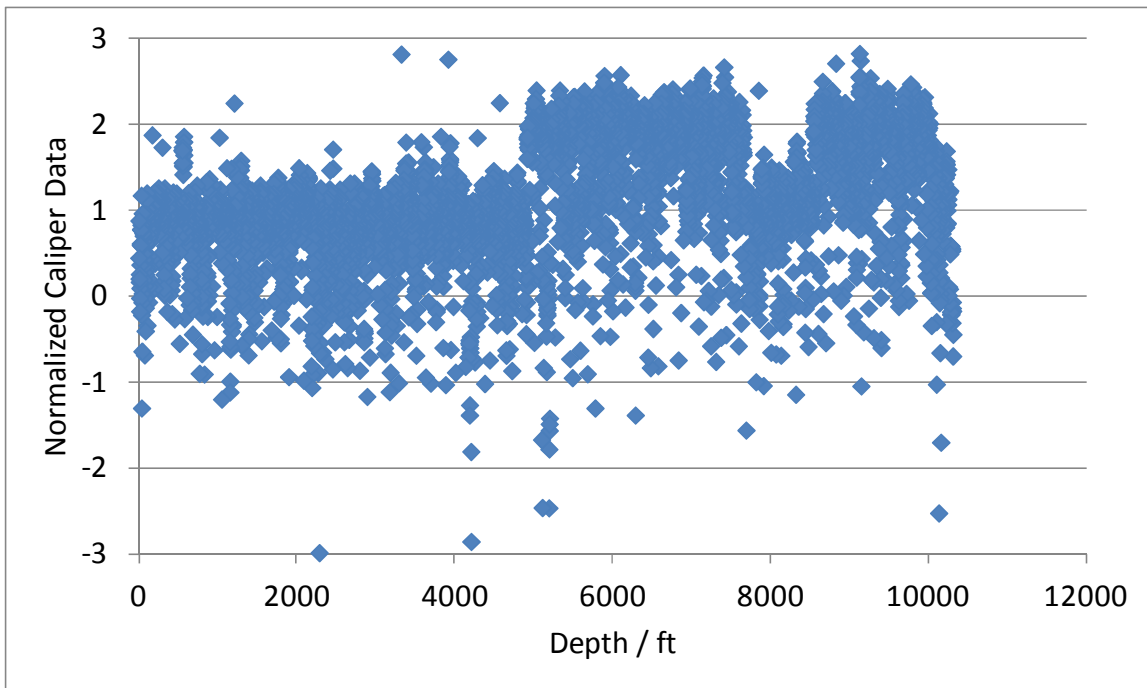


Figure 23: Normalized caliper data for Well B

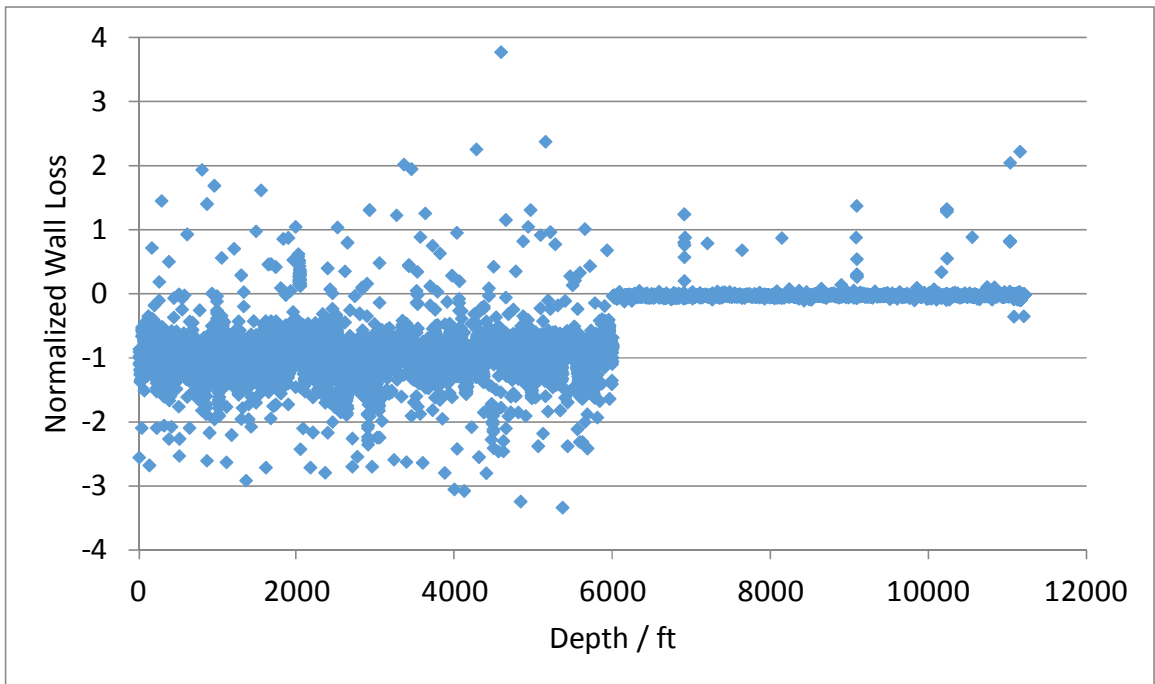


Figure 24: Normalized caliper data for Well C

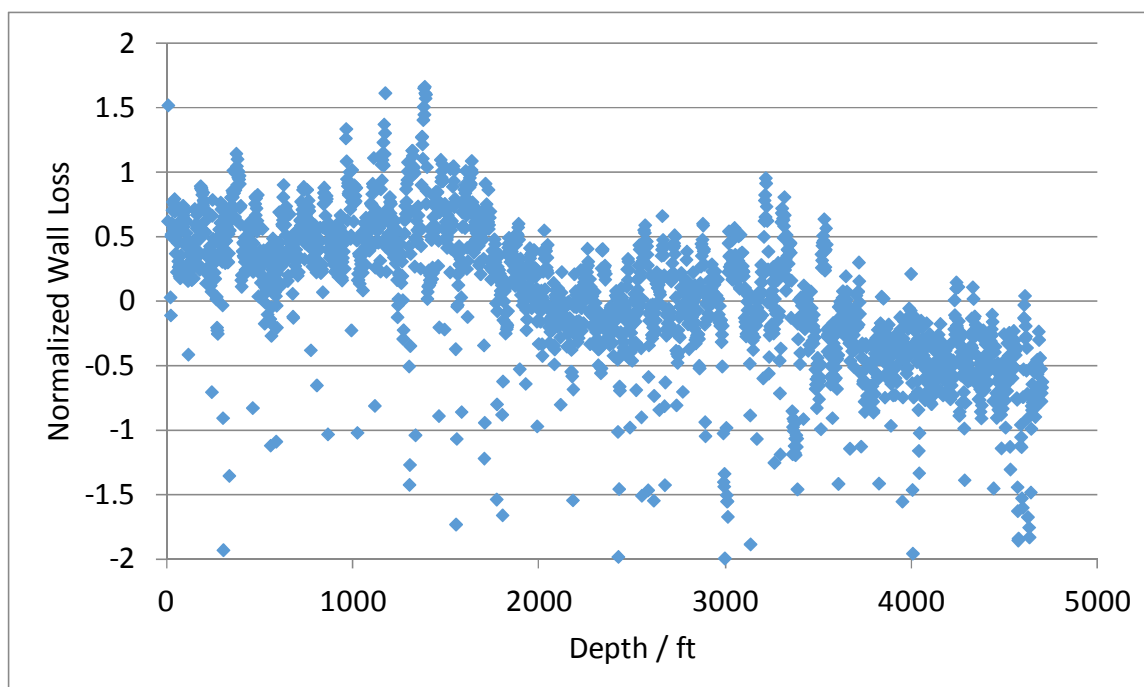


Figure 25: Normalized caliper data for Well D

#### 4.4.3 Model Results

The previous section discussed the overall trend of the caliper data, and in many cases the wall loss measurements were negative. For this section only the positive data were analyzed. WELLCORP does not attempt to predict gains in wall thickness due to scaling, so the negative caliper data were first removed, and then periodically sampled to get the final data set for model comparison. The caliper data allows for order-of-magnitude comparisons, thus it difficult declare which simulation was the most accurate.

The results for Well A are shown in Figure 26. The positive caliper data for this well have an overall flat trend, however, the model shows a distinct sloping trend with high wall loss at the bottomhole conditions. WELLCORP over-predicts the wall loss for the majority of Well A, but the simulated wall loss are on the same order of magnitude as

the caliper data. The overall caliper data for Well A showed wall gains in the first 2000 feet of tubing. Without scaling, the model and caliper data may have shown more similarity.

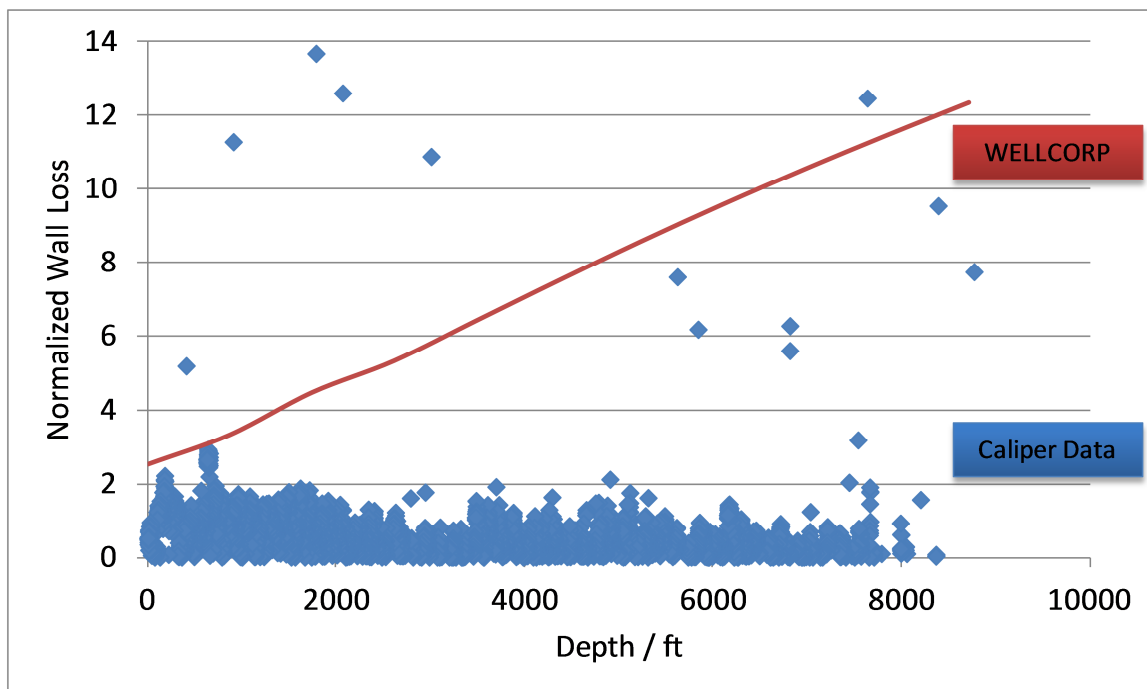


Figure 26: Normalized caliper and model results comparison for Well A.

The results for Well B (Figure 27) are similar to Well A. Again, the model over-predicts wall losses on the same order of magnitude as the caliper data. WELLCORP does show a similar downward sloping trend, but the slope is much steeper than that of the caliper data. Well B was also missing a few months of temperature and production data, so if there had been more data available the simulation may have been closer. Like Well A, there were signs of scaling in the caliper data, especially near the reservoir.

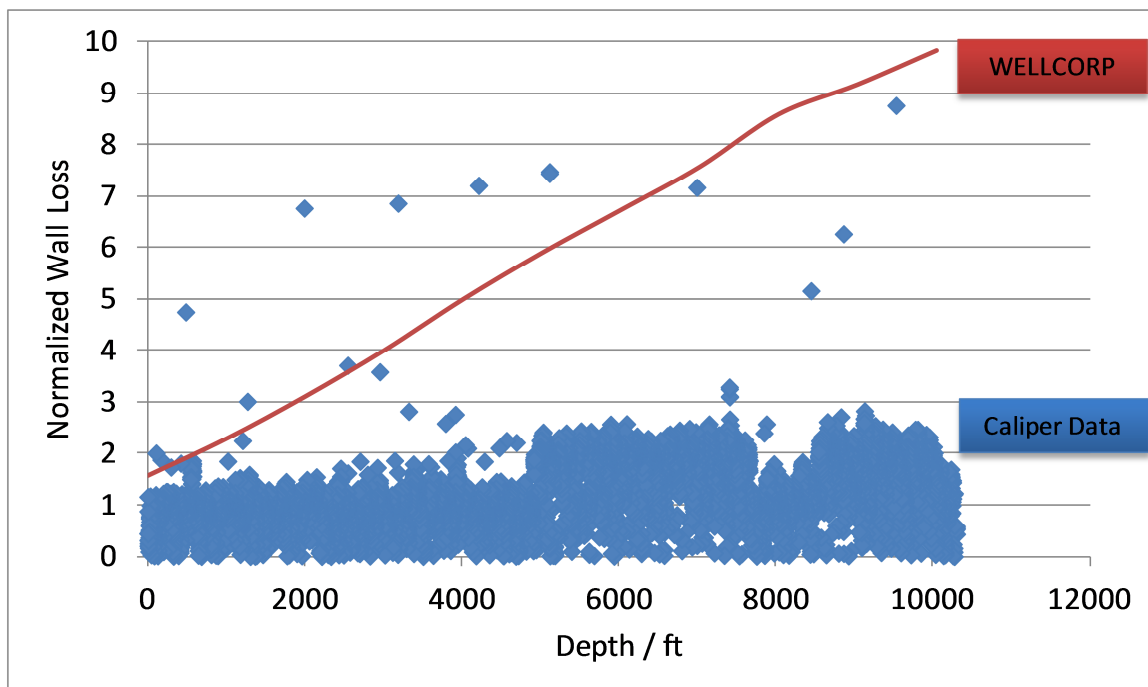


Figure 27: Normalized caliper and model results comparison for Well B.

The results for Well C (Figure 28) are within the scatter of the caliper data, and of the same order of magnitude as the majority of the data points. Well C had high negative wall losses, which resulted in fewer data points for comparison. However, the positive data compared better with the simulation results. In addition, Well C had less produced water than the other wells, which contributed to the lower predicted corrosion rates.

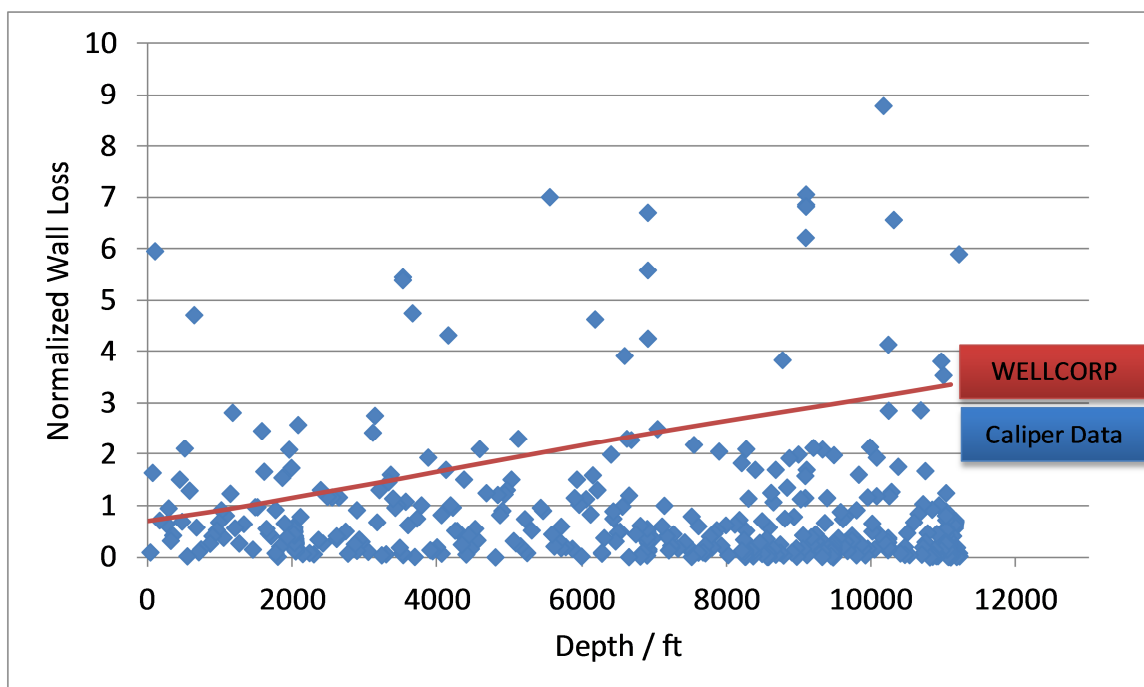


Figure 28: Normalized caliper and model results comparison for Well C.

The results for Well D, shown in Figure 29, are of the same order of magnitude as the caliper data. Well D also showed signs of significant scaling along the tubing, most heavily near the reservoir. This resulted in a lack of positive data points near the bottomhole. Of the four wells, Well D represented the best-case scenario in terms of data available, as it had the most complete compositional, temperature, pressure, and production data.

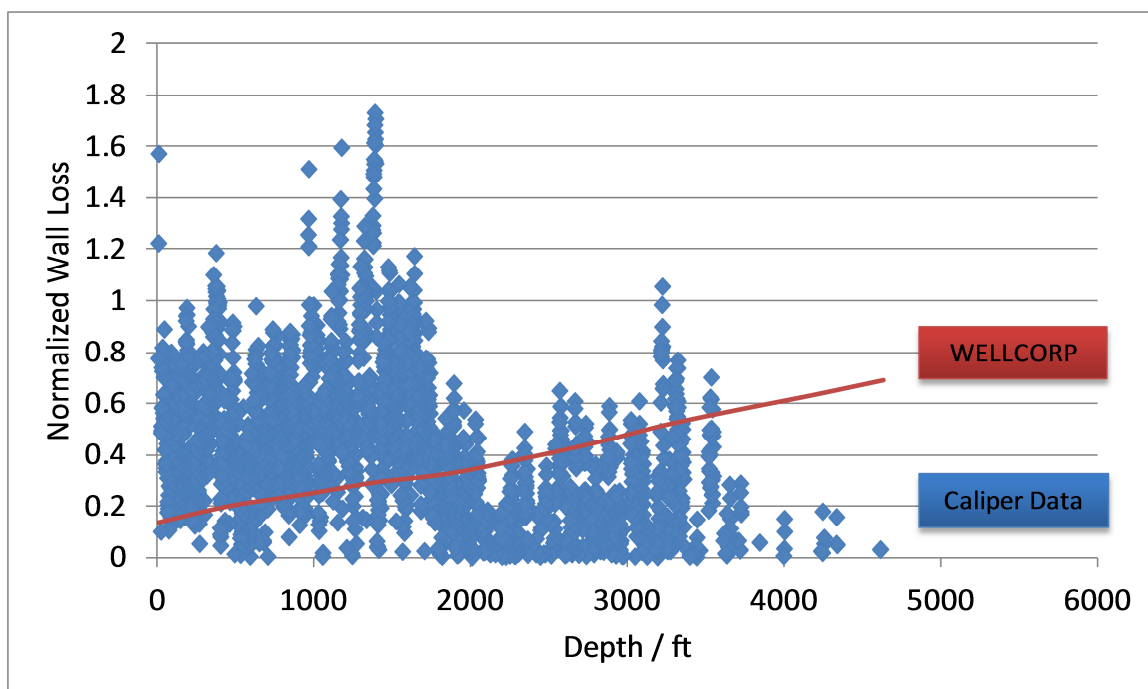


Figure 29: Normalized caliper and model results comparison for Well D

## 4.5 Summary

### 4.5.1 Model Limitations

A number of factors have not yet been taken into consideration by WELLCORP, and these factors limit the use of the model under certain circumstances. Major limitations associated with the current version of the model are listed below:

- This model predicts uniform corrosion; no localized corrosion module is presently included.
- This model employs a simple empirical correlation based on super-saturation of iron carbonate to simulate iron carbonate film growth, which is subject to further development.

- This model does not take into account the effect of high solution salinity on the corrosion process.
- A simple criterion is used to determine the transition between CO<sub>2</sub> dominated and H<sub>2</sub>S dominated corrosion. When CO<sub>2</sub> and H<sub>2</sub>S coexist, corrosion rates are calculated based on the CO<sub>2</sub> and H<sub>2</sub>S corrosion mechanism described earlier. The corrosion rates are then compared with each other. The mechanism that gives the higher corrosion rate is considered the dominant mechanism.

#### 4.5.2 Model Achievements

- A corrosion model for production tubing was created using an improved version of ICMT's FREECORP as a base model. The improved model accounted for phase non-idealities by including an activity model, fugacity model, and semi-empirical solubility models.
- The improved point model compared better with experimental results than the original FREECORP model in all cases, and reduced predictions by close to 40 percent at 80 bar CO<sub>2</sub>.
- The four sets of field data simulations compared reasonable well with caliper data (within the same order of magnitude).
- Scaling likely interfered with caliper readings, resulting in inaccurately measured wall losses.

## CHAPTER 5: THERMOCORP

The corrosion product is an important factor in corrosion rate prediction. Some products can provide protection, such as magnetite ( $\text{Fe}_3\text{O}_4$ ), while other products do not. Pourbaix diagrams allow for prediction of formation of these corrosion products. ThermoCORP was developed to facilitate easy and quick calculation of Pourbaix diagrams. Additionally, it was designed to be an open source learning tool for students. The following sections detail the methodology behind the ThermoCORP program and compare the results of ThermoCORP with that of OLI Analyzer Studio, one of the leading industrial providers of thermodynamic prediction software.

### 5.1 Methodology

The most common approach to create Pourbaix diagrams is to use the Nernst equation (Equation 48). This will give an equation for potential that is a function of temperature and species concentration, which, when plotted, gives a straight line. The user or a program must then decide where one line ends and another begins.

$$E_{rev} = E_{rev}^o - \frac{RT}{zF} \log \left( \frac{C_{red}}{C_{ox}} \right) \quad (48)$$

Where:

$E_{rev}$ : Reversible potential, V;

$E_{rev}^o$ : Standard reversible potential, V;

$z$ : Number of electrons exchanged;

$R$ : Universal gas constant, J/mol·K;

$T$ : Absolute temperature, K;

$F$ : Faraday's constant;

$C_{red}$ : Concentration of the reduced species;

$C_{ox}$ : Concentration of the oxidized species.

ThermoCORP is based on the principle that the species with the lowest Gibb's free energy is the most stable, and thus should be the species present. The methodology used in ThermoCORP is adapted from that of Fishtik [47]. Furthermore, the underlying thermodynamic data is based on the work of Tanupabrungsun and Ning et al. [25], [26]. It performs the task of creating a Pourbaix diagram differently than the common approach, however, in that it calculates the most stable species at every point. The transition lines appear as a boundary between different stability regions. Equation 49 shows an example of a change in Gibb's free energy ( $\Delta G$ ) calculation for iron oxidizing to ferrous ions. Each species also has a temperature dependence that is derived from heat capacity [47].

$$\Delta G_{Fe \rightarrow Fe^{2+}} = \frac{-(G_{Fe} - G_{Fe^{2+}})}{F} - 2E + \frac{RT}{F} \ln([Fe^{2+}]) \quad (49)$$

Where:

$G_{Fe}$ ,  $G_{Fe^{2+}}$ : Gibbs free energy of Fe and  $Fe^{2+}$  respectively;

$E$ : Potential, V;

$[Fe^{2+}]$ : Concentration of  $Fe^{2+}$ , mol/L

To calculate the most stable species at a given point, a vector made up of the  $\Delta G$  values for each reaction of iron going to another species (i.e., iron to ferrous ion, iron to iron carbonate, etc.) is multiplied by the stoichiometric matrix. This yields the Gibb's free energy for each species (Equation 50). With this calculation completed, the species

that has the lowest Gibb's free energy is considered the most stable, and is most likely to be present at that potential and pH.

$$\begin{bmatrix} \Delta G_{Fe-Fe^{2+}} \\ \Delta G_{Fe-Fe^{3+}} \\ \Delta G_{Fe-Fe_2O_3} \\ \Delta G_{Fe-FeS} \end{bmatrix} \cdot \begin{bmatrix} -1 & 1 & 0 & 0 & 0 \\ -1 & 0 & 1 & 0 & 0 \\ -1 & 0 & 0 & 1 & 0 \\ -1 & 0 & 0 & 0 & 1 \end{bmatrix} = \begin{bmatrix} G_{Fe} \\ G_{Fe^{2+}} \\ G_{Fe^{3+}} \\ G_{Fe_2O_3} \\ G_{FeS} \end{bmatrix} \quad (50)$$

Since the  $\Delta G$  values are now functions of potential (E) and pH, a point-by-point calculation can be performed. This provides a benefit over traditional Pourbaix diagrams, in that a single point can be calculated. This allows ThermoCORP to interface with WELLCORP, or any other Visual Basic based software, and to provide analysis at a single point to see which phase is stable at those conditions. Currently, this program works for pure CO<sub>2</sub>, pure H<sub>2</sub>S, and a mixed system of CO<sub>2</sub> and H<sub>2</sub>S for 25-300°C. The hard limits for H<sub>2</sub>S and CO<sub>2</sub> are a check to ensure that species are not supercritical at the specified conditions.

## 5.2 Interface and Design

ThermoCORP is split into two main modules, the Pourbaix diagram module, and the "slice" module. The Pourbaix diagram module generates a potential-pH stability diagram (Figure 30). The example shown in Figure 30 is for a pure H<sub>2</sub>S system. The Pourbaix diagram can have any range of potential between  $\pm 2$  V or pH between 0 and 14. It also allows for turning on and off different polymorphs of iron sulfide.

The "slice" diagram generates a stability diagram for varied Fe<sup>2+</sup> concentration, temperature, partial pressure of CO<sub>2</sub>, or partial pressure of H<sub>2</sub>S *versus* pH (Figure 31)

while all other parameters remain constant. Figure 31 shows an example for a pure H<sub>2</sub>S system with varied pH and temperature.

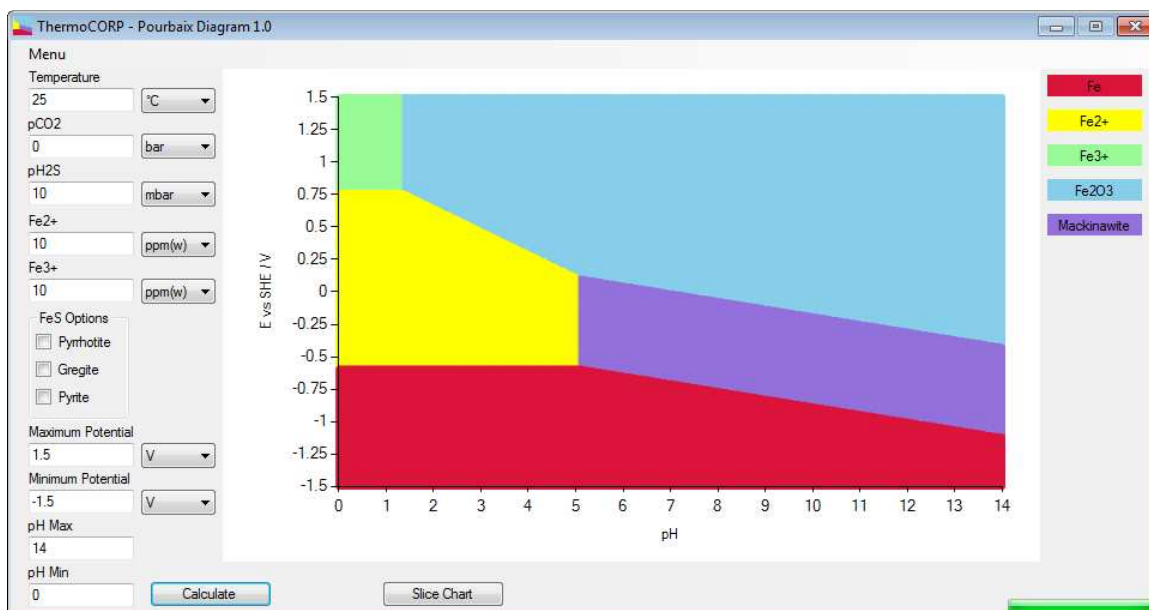


Figure 30: Pourbaix diagram interface. An example is shown for a pure H<sub>2</sub>S system.

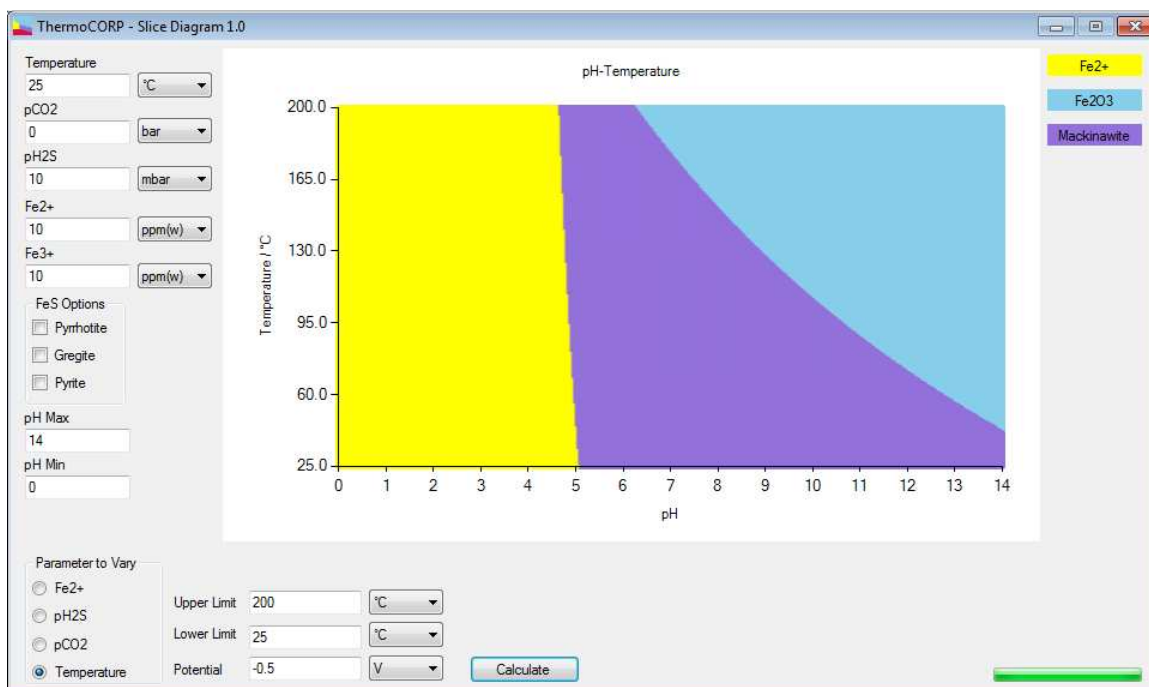


Figure 31: "Slice" diagram interface. Shown is an example for a pure H<sub>2</sub>S system with varied temperature.

### 5.3 Results and Discussion

ThermoCORP compares well with the previous work at ICMT, which is to be expected since it is based on the same set of reference equations. A more interesting comparison is the of ThermoCORP with a well-known program like OLI. The next set of figures show some comparisons between OLI and ThermoCORP. The overlaid blue lines are the results of OLI for the same system.

Figure 32 and Figure 33 show Pourbaix diagrams from an Fe-H<sub>2</sub>O system at 25°C and 80°C, respectively. The results at 25°C agree; any differences result from variances between standard Gibb's free energy values. At 80°C, OLI begins to introduce species not considered in ThermoCORP, such as FeOH<sup>2+</sup> and Fe(OH)<sub>4</sub><sup>-</sup>, which interferes with the

$\text{Fe}^{3+}$  and  $\text{Fe}_3\text{O}_4$  areas. For this simple iron-water system the results were comparable, with similar predictions.

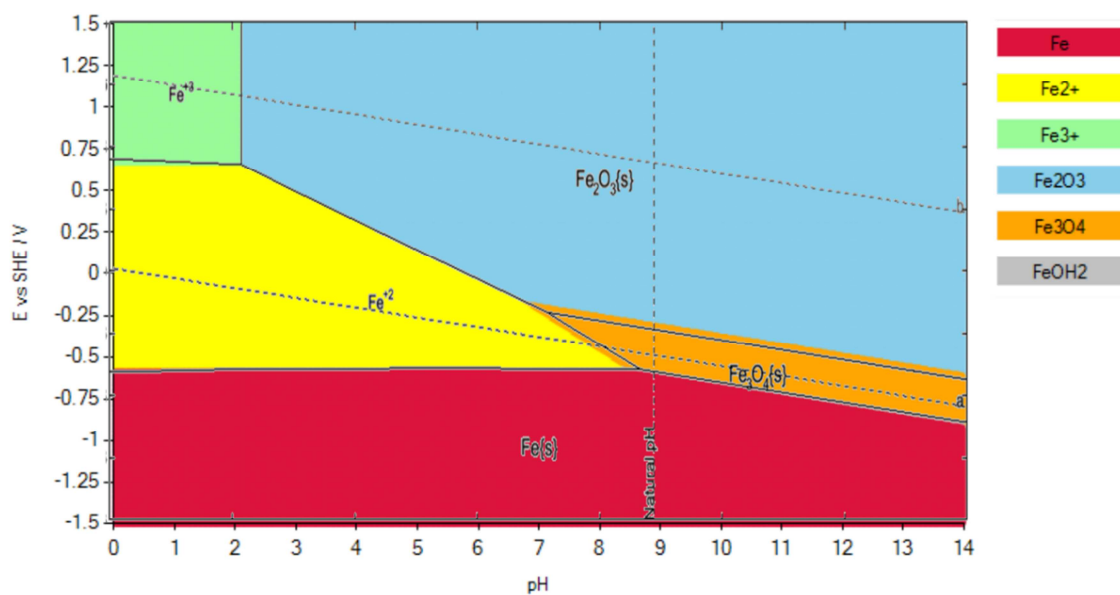


Figure 32: Pourbaix diagram comparison for an Fe-H<sub>2</sub>O system at 25°C,  $[\text{Fe}^{2+}] = 10 \text{ ppm}$ ,  $[\text{Fe}^{3+}] = 10^{-6} \text{ mol/L}$

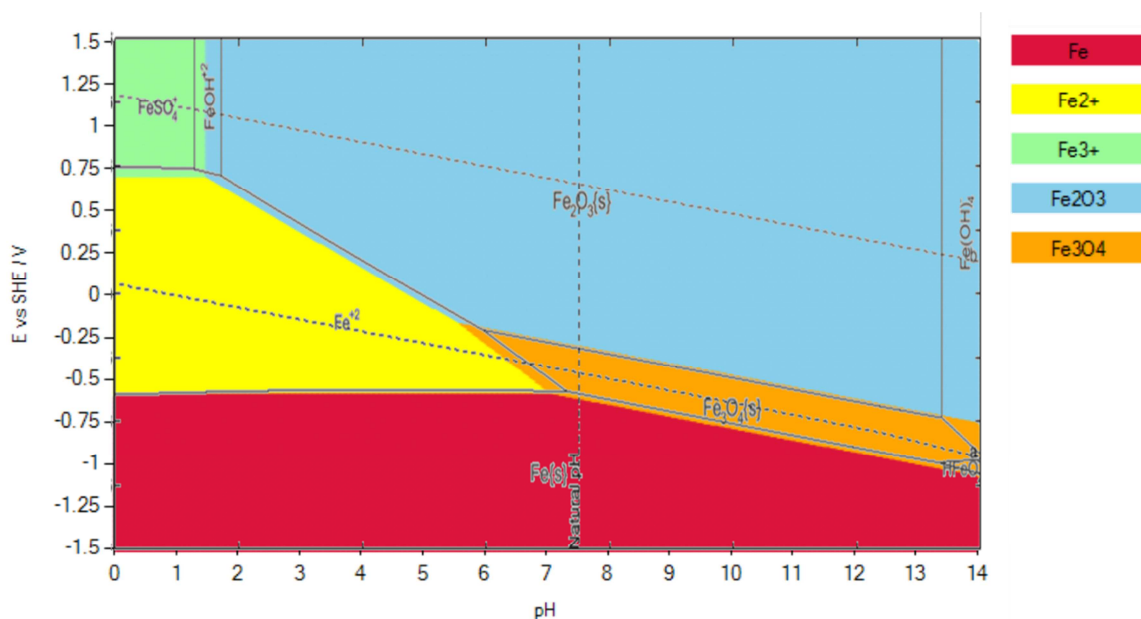


Figure 33: Pourbaix diagram comparison for an Fe-H<sub>2</sub>O system at 80°C, [Fe<sup>2+</sup>]=10ppm, [Fe<sup>3+</sup>]=10<sup>-6</sup> mol/L

Figure 34, Figure 35 and Figure 36 show Pourbaix diagrams for an Fe-H<sub>2</sub>O-H<sub>2</sub>S system at 25°C, 80°C, and 250°C, respectively. For this comparison, even at 25°C the diagrams are quite different. This is likely because OLI accounts for pressure effects, while ThermoCORP does not. In addition, like the Fe-H<sub>2</sub>O system, OLI introduces more species to the Pourbaix diagram. At 25°C and 80°C, OLI and ThermoCORP produced Pourbaix diagrams of a comparable nature. At 250°C, however, results were very different, as is apparent in the overlay. Again, this is likely due to OLI accounting for pressure effects, and introducing complex species. At 80°C and 250°C OLI predicts FeSO<sub>4</sub><sup>+</sup> rather than Fe<sup>3+</sup>. This is because OLI takes into account the titrants used, in this case sulfuric acid and sodium hydroxide.

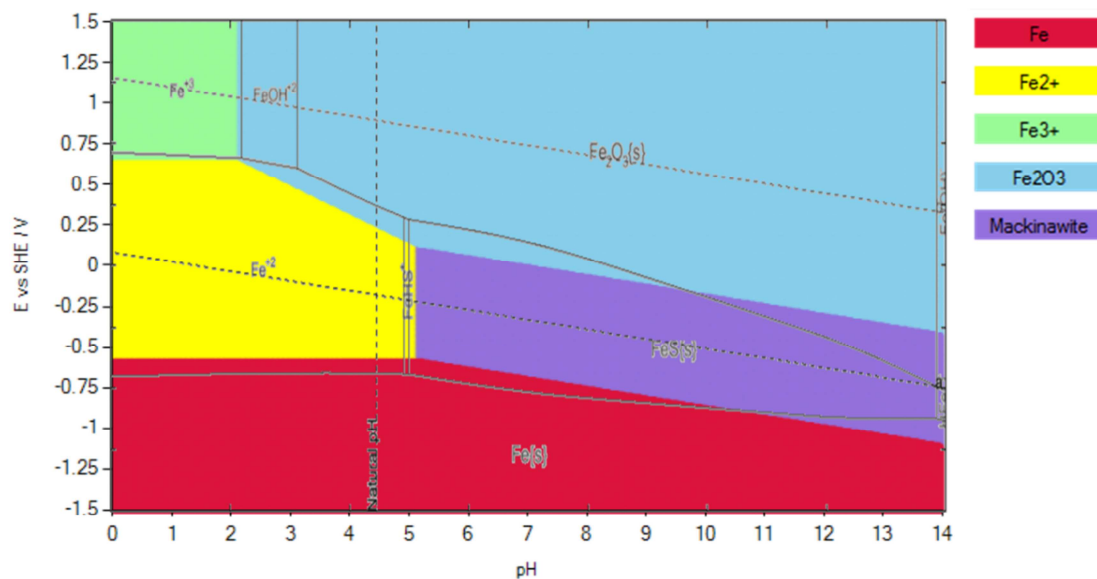


Figure 34: Pourbaix diagram comparison for an Fe-H<sub>2</sub>O-H<sub>2</sub>S system at 25°C, 10% H<sub>2</sub>S, [Fe<sup>2+</sup>]=10ppm, [Fe<sup>3+</sup>]=10<sup>-8</sup> mol/L

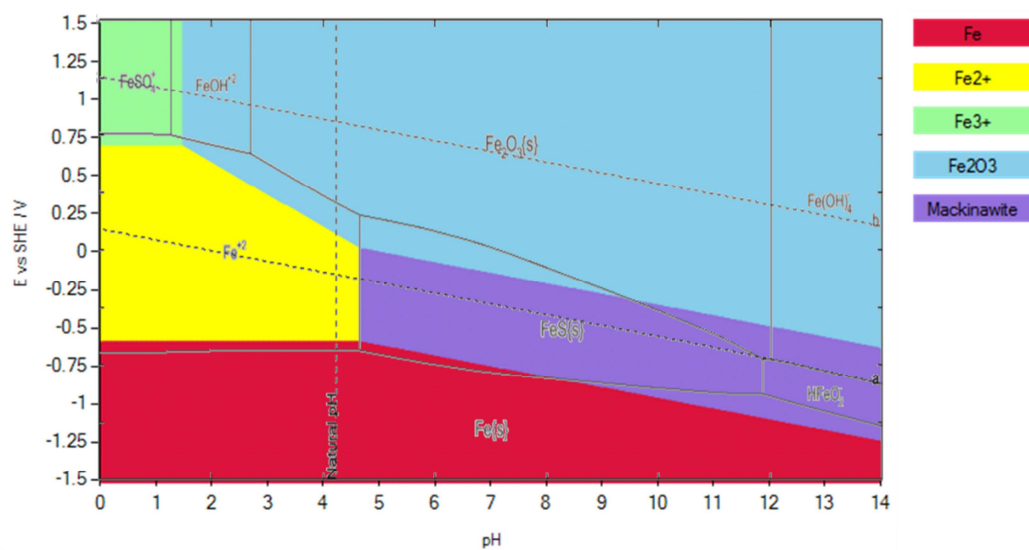


Figure 35: Pourbaix diagram comparison for an Fe-H<sub>2</sub>O-H<sub>2</sub>S system at 80°C, 10% H<sub>2</sub>S, [Fe<sup>2+</sup>]=10ppm, [Fe<sup>3+</sup>]=10<sup>-8</sup> mol/L.

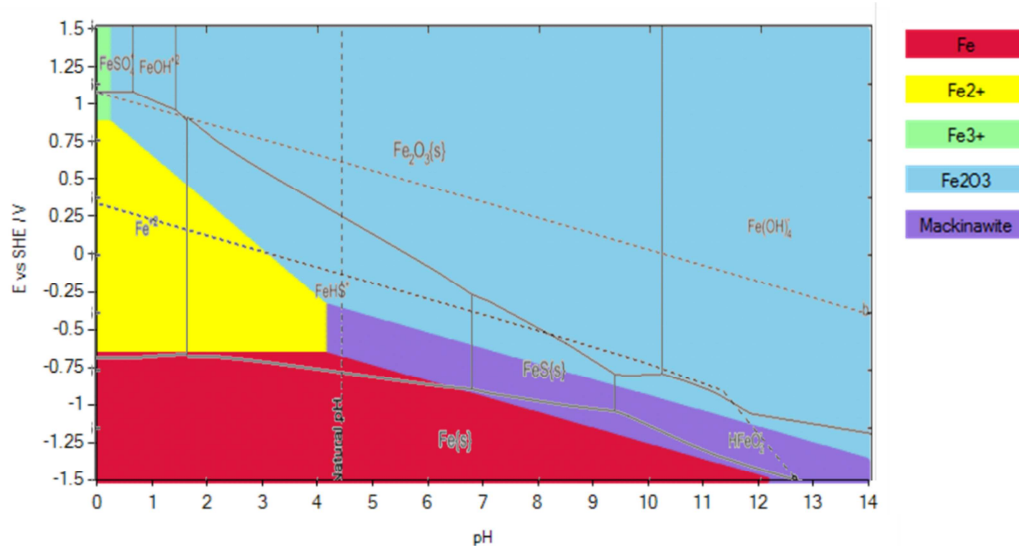


Figure 36: Pourbaix diagram comparison for an Fe-H<sub>2</sub>O-H<sub>2</sub>S system at 250°C, 10% H<sub>2</sub>S, [Fe<sup>2+</sup>]=10ppm, [Fe<sup>3+</sup>]=10<sup>-8</sup> mol/L.

The Pourbaix diagrams for an Fe-H<sub>2</sub>O-CO<sub>2</sub> system at 25°C, 80°C, and 250°C are shown in Figure 37, Figure 38, and Figure 39 respectively. The overlay comparisons between ThermoCORP and OLI are quite close for the CO<sub>2</sub> system. The shape of the iron carbonate (FeCO<sub>3</sub>) sections in 25°C and 80°C diagrams are slightly different. This is due in part to the presence of magnetite (Fe<sub>3</sub>O<sub>4</sub>) on the OLI generated diagram. Similarly to shown for the H<sub>2</sub>S system, Fe<sup>3+</sup> is replaced by FeSO<sub>4</sub><sup>+</sup> above 80°C. At 250°C the two generated Pourbaix diagrams have very similar shapes, though the lines were off by 0.25 V. Overall, the CO<sub>2</sub> system compared well with OLI.

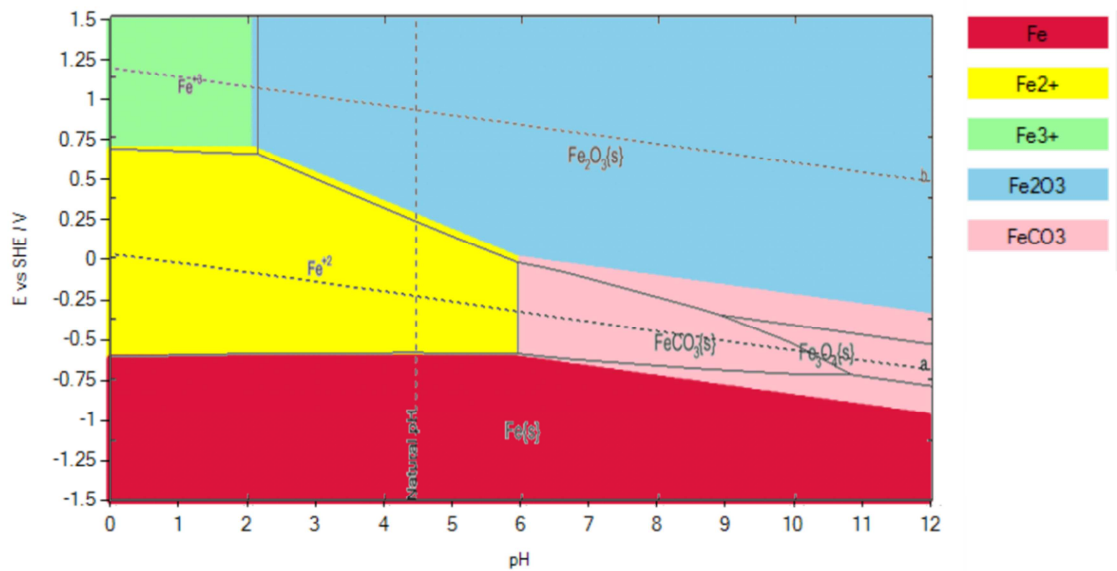


Figure 37: Pourbaix diagram comparison for an Fe-H<sub>2</sub>O-CO<sub>2</sub> system 25°C, 1 bar CO<sub>2</sub>, [Fe<sup>2+</sup>]=10ppm, [Fe<sup>3+</sup>]=10<sup>-6</sup> mol/L

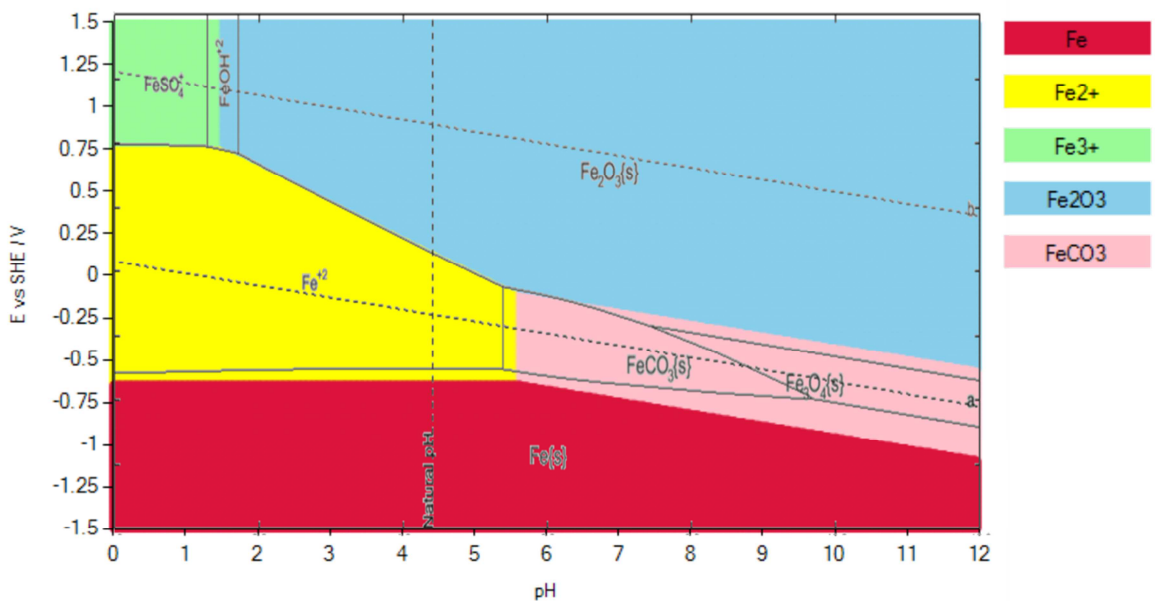


Figure 38: Pourbaix diagram comparison for an Fe-H<sub>2</sub>O-CO<sub>2</sub> system 80°C, 2.21 bar CO<sub>2</sub>, [Fe<sup>2+</sup>]=10ppm, [Fe<sup>3+</sup>]=10<sup>-6</sup> mol/L

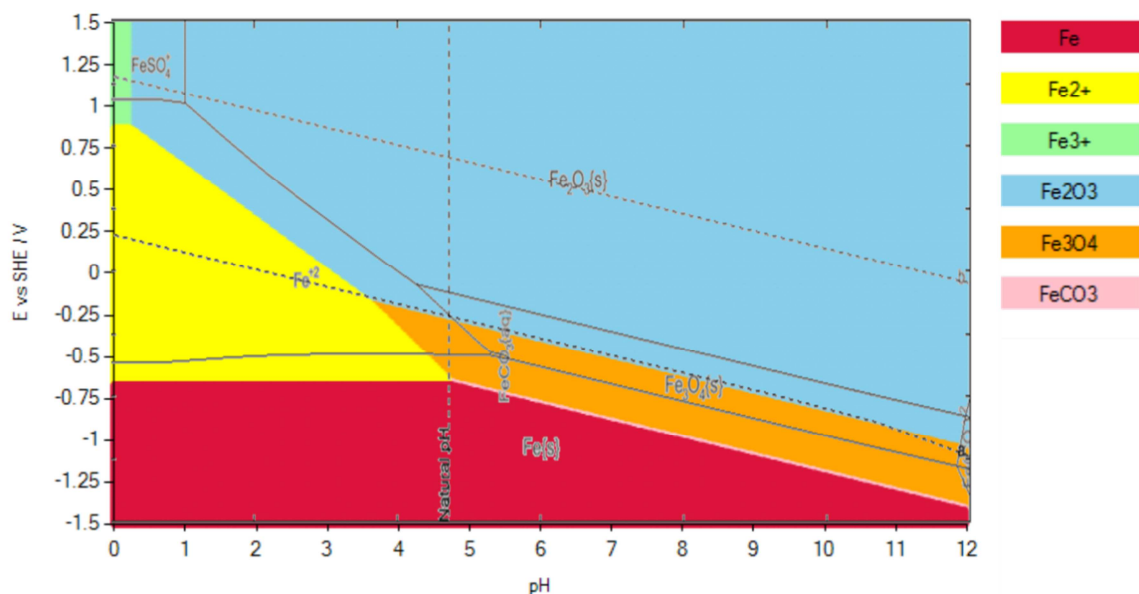


Figure 39: Pourbaix diagram comparison for an Fe-H<sub>2</sub>O-CO<sub>2</sub> system 250°C, 2.43 bar CO<sub>2</sub>, [Fe<sup>2+</sup>]=10ppm, [Fe<sup>3+</sup>]=10<sup>-6</sup> mol/L

#### 5.4 Summary

- An easy-to-use tool called ThermoCORP has been created based on the open literature to facilitate the creation of Pourbaix diagrams.
- ThermoCORP allows for generation of diagrams containing different FeS species in order to understand the transient nature of the iron sulfides. ThermoCORP always considers mackinawite, but allows for selection of any or all of the following: pyrrhotite, greigite, and pyrite.
- The ThermoCORP program can generate a “slice” into the Pourbaix diagram at a given potential by varying a parameter such as pCO<sub>2</sub>, pH<sub>2</sub>S, temperature, or Fe<sup>2+</sup> concentration in order to analyze the effect of changing environmental parameters.

- ThermoCORP results compare well with the well-known thermodynamic package, OLI Analyzer.

## CHAPTER 6: CONCLUSIONS AND FUTURE WORK

### 6.1 Conclusions

The FREECORP model was improved by accounting for non-idealities in the gas and liquid phases, as well as new solubility models for both H<sub>2</sub>S and CO<sub>2</sub>. The improved version of FREECORP showed an improvement over the original model when compared to experimental data.

Using the improved FREECORP, a new line model called WELLCORP was created for calculating corrosion along production tubing. Four different wells were simulated with the WELLCORP model, and then compared with caliper measurements. All four cases compared reasonably well, with calculated wall losses on the same order of magnitude as the caliper data. In all cases, scaling of the tubing likely interfered with the true wall loss measurements. In addition, the lack of regular measurement added to the discrepancies between the measured and simulated wall losses.

An additional thermodynamic model was created, called ThermoCORP, to facilitate the creation of Pourbaix diagrams. This model forms the basis of the corrosion production stability calculation in WELLCORP. ThermoCORP was compared with OLI, a widely used comprehensive thermodynamic package. The comparisons for the Fe-H<sub>2</sub>O system showed agreement. The results for an Fe-H<sub>2</sub>O-H<sub>2</sub>S system did not compare as well as the other two systems, due to the extra species added by OLI. The Fe-H<sub>2</sub>O-CO<sub>2</sub> system had similar shapes; however, the equilibrium lines were shifted slightly in each case.

## 6.2 Future Work

- Compare WELLCORP with more fields to verify wall loss prediction values.
- Verify WELLCORP with long-term vertical flow loop tests.
- Add the sulfide stress cracking (SSC) check as an optional calculation into WELLCORP.
- Integrate WELLCORP and ThermoCORP to predict the transition from CO<sub>2</sub> dominated corrosion to H<sub>2</sub>S dominated corrosion.

## REFERENCES

- [1] M. B. Kermani and A. Morshed, "Carbon dioxide corrosion in oil and gas production—A compendium," *Corrosion*, vol. 59, no. 8, pp. 659–683, Aug. 2003.
- [2] S. Nešić, J. Postlethwaite, and S. Olsen, "An electrochemical model for prediction of corrosion of mild steel in aqueous carbon dioxide solutions," *Corrosion*, vol. 52, no. 4, pp. 280–294, 1996.
- [3] M. Nordsveen, S. Nešić, R. Nyborg, and A. Stangeland, "A mechanistic model for carbon dioxide corrosion of mild steel in the presence of protective iron carbonate films — Part 1: Theory and verification," *Corrosion*, vol. 59, no. 5, pp. 443–456, 2003.
- [4] S. Nešić, M. Nordsveen, R. Nyborg, and A. Stangeland, "A mechanistic model for carbon dioxide corrosion of mild steel in the presence of protective iron carbonate films — Part 2: A numerical experiment," *Corrosion*, vol. 59, no. 6, pp. 489–497, 2003.
- [5] S. Nešić and K.-L. J. Lee, "A mechanistic model for carbon dioxide corrosion of mild steel in the presence of protective iron carbonate films — Part 3: Film growth model," *Corrosion*, vol. 59, no. 7, pp. 616–628, 2003.
- [6] C. de Waard and D. E. Milliams, "Carbonic acid corrosion of steel," *Corrosion*, vol. 31, no. 5, pp. 177–182, 1975.
- [7] C. de Waard and D. E. Milliams, "Prediction of carbonic acid corrosion in natural gas pipelines," *First International Conference on the Internal and External Protection of Pipes*, no. F1, pp. 1–8, 1975.
- [8] C. de Waard and U. Lotz, "Prediction of CO<sub>2</sub> corrosion of carbon steel," *CORROSION/93*, 1993, no. 69, pp. 1–17.
- [9] C. de Waard, U. Lotz, and A. Dugstad, "Influence of liquid flow velocity on CO<sub>2</sub> corrosion: A semi-empirical model," *CORROSION/95*, 1995, no. 128, pp. 1–14.
- [10] S. Nešić, H. Li, J. Huang, and D. Sormaz, "An open source mechanistic model for CO<sub>2</sub>/H<sub>2</sub>S corrosion of carbon steel," *CORROSION/09*, 2009, no. 09572, pp. 1–19.
- [11] Y. Zheng, B. Brown, and S. Nešić, "Electrochemical study and modeling of H<sub>2</sub>S corrosion of mild steel," *Corrosion*, vol. 70, no. 4, pp. 351–365, 2014.
- [12] S. N. Smith and R. Pakalapati, "Thirty years of downhole corrosion experience at Big Escambia Creek: Corrosion mechanisms and inhibition," *CORROSION/04*, 2004, no. 04744, pp. 1–17.

- [13] J. Manocha and T. Carter, "Oil and gas exploration, production and legislation on Ontario farms," 1999.
- [14] G. Schmitt and B. Rothmann, "Studies on the corrosion mechanism of unalloyed steel in oxygen-free carbon dioxide solutions. Part I - Kinetics of the liberation of hydrogen," *Werkstoffe und Korrosion*, vol. 28, 1977.
- [15] Y. Yang, B. Brown, S. Nešić, M. E. Gennaro, and B. Molinas, "Mechanical strength and removal of a protective iron carbonate layer formed on mild steel in CO<sub>2</sub>," *CORROSION/10*, 2010, no. 10383, pp. 1–19.
- [16] B. Pots, "Mechanistic models for the prediction of CO<sub>2</sub> corrosion rates under multi-phase flow conditions," *CORROSION/95*, 1995, no. 137, pp. 1–20.
- [17] G. M. Abriam, "Controlling corrosion of carbon steel in sweet high temperature and pressure downhole environments with the use of corrosion inhibitors," *NACE Northern Area Western Conference*, 2010.
- [18] O. Shoham, *Mechanistic Modeling of Gas-Liquid Two-Phase Flow in Pipes*. Society of Petroleum Engineers, 2006.
- [19] H. Fang, "Low temperature and high salt concentration effects on general CO<sub>2</sub> corrosion for carbon steel," M.S. thesis, Ohio University, Athens, OH, 2006.
- [20] J. D. Hem, *Study and Interpretation of the Chemical Characteristics of Natural Water*, 3rd ed. U.S. Geological Survey, 1985, p. 106.
- [21] S. Wang, K. George, and S. Nešić, "High pressure CO<sub>2</sub> corrosion electrochemistry and the effect of acetic acid," *CORROSION/04*, 2004, no. 04375, pp. 1–17.
- [22] ICMT, "FREECORP Background." [Online]. Available: <http://www.corrosioncenter.ohiou.edu/software/freecorp/pdfs/FREECORP-Background.pdf>. [Accessed: 26-Mar-2013].
- [23] S. Nešić, S. Wang, H. Fang, W. Sun, and J. K.-L. Lee, "A new updated model of CO<sub>2</sub>/H<sub>2</sub>S corrosion in multiphase flow," *CORROSION/08*, 2008, no. 08535, pp. 1–16.
- [24] W. Sun, S. Nešić, and R. C. Woollam, "The effect of temperature and ionic strength on iron carbonate (FeCO<sub>3</sub>) solubility limit," *Corros. Sci.*, vol. 51, no. 6, pp. 1273–1276, Jun. 2009.

- [25] T. Tanupabrungsun, D. Young, B. Brown and S. Nešić, “Construction and verification of pourbaix diagrams for CO<sub>2</sub> corrosion of mild steel valid up to 250°C,” *CORROSION/12*, 2012, no. 01418, pp 1-16.
- [26] J. Ning, Y. Zheng, D. Young, B. Brown, and S. Nešić, “Thermodynamic study of hydrogen sulfide corrosion of mild steel,” *Corrosion*, vol. 70, no. 4, pp. 375–389, 2014.
- [27] W. Sun and S. Nešić, “A mechanistic model of H<sub>2</sub>S corrosion of mild steel,” *CORROSION/07*, 2007, no. 07655, pp. 1–26.
- [28] E. Akeer, B. Brown, and S. Nešić, “The influence of steel metallurgy on the initiation of localized CO<sub>2</sub> corrosion caused by varying flow conditions,” *CORROSION/13*, 2013, no. 2383, pp. 1-16.
- [29] B. D. Craig, “Metallurgy for Oil and Gas Production,” in *Practical Oilfield Metallurgy and Corrosion*, 2nd ed., Denver, CO: PennWell, 1993, pp. 131–141.
- [30] “NACE MR0175/ISO 15156 Petroleum and natural gas industries — Materials for use in H<sub>2</sub>S-containing environments in oil and gas production,” 2001.
- [31] C. Mendez, S. Duplat, S. Hernandez, and J. Vera, “On the mechanism of corrosion inhibition by crude oils,” *CORROSION/01*, 2001, no. 01044, pp. 1–19.
- [32] K. Pedersen and P. Christensen, “Flash and phase envelope calculations,” in *Phase Behavior of Petroleum Reservoir Fluids*, 2007, pp. 115–140.
- [33] D.-Y. Peng and D. B. Robinson, “A new two-constant equation of state,” *Ind. Eng. Chem. Fundam.*, vol. 15, no. 1, pp. 59–64, Feb. 1976.
- [34] K. S. Pitzer, “Thermodynamics of electrolytes I. Theoretical basis and general equations,” *J. Phys. Chem.*, vol. 7242, no. 6, pp. 268–277, 1972.
- [35] K. S. Pitzer and G. Mayorga, “Thermodynamics of electrolytes II. Activity and osmotic coefficients for strong electrolytes with one or both ions univalent,” *J. Phys. Chem.*, vol. 77, no. 19, pp. 2300–2308, 1973.
- [36] R. Nyborg, “Field data collection, evaluation and use for corrosivity prediction and validation of models - Part II: Evaluation of field data and comparison of prediction models,” *CORROSION/06*, 2006, no. 06118, pp. 1–15.
- [37] C. Plennevaux, T. Cassagne, M. Bonis, J. Kittel, F. Ropital, N. Ferrando, M. Fregonese, and B. Normand, “Improving pH prediction for high pressure and high

- temperature applications in oil and gas production,” *CORROSION/13*, 2013, no. 2843, pp. 1–14.
- [38] Y. Gunaltun and A. Kopluku, “Field data collection, evaluation and use for corrosivity prediction and validation of models - Part I: Collection of reliable field data for validation of prediction models,” *CORROSION/06*, 2006, no. 06117, pp. 1–18.
- [39] Z. Duan and R. Sun, “An improved model calculating CO<sub>2</sub> solubility in pure water and aqueous NaCl solutions from 273 to 533 K and from 0 to 2000 bar,” *Chem. Geol.*, vol. 193, no. 3–4, pp. 257–271, Feb. 2003.
- [40] J. Oddo and M. Tomson, “Simplified calculation of CaCO<sub>3</sub> saturation at high temperatures and pressures in brine solutions,” *J. Pet. Technol.*, pp. 1583–1590, 1982.
- [41] Z. Duan, R. Sun, R. Liu, and C. Zhu, “Accurate thermodynamic model for the calculation of H<sub>2</sub>S solubility in pure water and brines,” no. 13, pp. 2056–2065, 2007.
- [42] E. Hogfeldt, *IUPAC, Stability Constants of Metal-Ion Complexes, Part A: Inorganic Ligands*. Oxford, U.K., 1982.
- [43] J. J. Carroll, “The water content of acid gas and sour gas from 100 ° to 220 ° F and pressures to 10,000 psia . Part 1 – Pure components,” *81st Annual GPA Convention*, 2002.
- [44] N. Jauseau, “Multiphase flow effects on naphthenic acid corrosion of carbon steel,” Ohio University, 2012.
- [45] S. K. Srivastava, B. Kumar, S. R. Prasad, and S. K. Sahota, “Failure analysis of oil and gas production tubing in an inclined well,” *Mater. Perform.*, no. November, pp. 58–62, 2013.
- [46] A. M. Nor, M. Suhor, M. Mohamed, M. Singer, and S. Nešić, “Corrosion of carbon steel in high CO<sub>2</sub> environment: Flow effect,” *CORROSION/11*, 2011, vol. 0, no. 11242.
- [47] I. Fishtik, “Thermodynamic stability relations in redox systems,” *Environ. Sci. Technol.*, vol. 40, no. 6, pp. 1902–10, Mar. 2006.



**OHIO**  
UNIVERSITY

Thesis and Dissertation Services